



TECHNISCHE
UNIVERSITÄT
WIEN

DIPLOMARBEIT

Implementation of a combined optical system for versatile generation of dipole potential

zur Erlangung des akademischen Grades
Diplom-Ingenieur

ausgeführt am Atominstitut
der Technischen Universität Wien

Institute of Atomic and Subatomic Physics
Vienna University of Technology

unter der Anleitung von
Univ.Prof. Dipl.-Ing. Dr.tech. Hannes-Jörg Schmiedmayer
und
Projektass. RuGway Wu PhD

durch

Lukas Leczek BSc
Matrikelnummer: 01604877

Hannes-Jörg Schmiedmayer

Lukas Leczek

Wien, February 1, 2024



Die approbierte gedruckte Originalversion dieser Diplomarbeit ist an der TU Wien Bibliothek verfügbar
The approved original version of this thesis is available in print at TU Wien Bibliothek.

Abstract

In this thesis an optical system, combining an adjustable ring pattern created by axicon lenses and tailored light patterns created with a digital micro-mirror device (DMD) was designed and realized. This system will be integrated into a ${}^6\text{Li}$ cold quantum gas experiment.

In the first part improved ray-tracing matrices for axicon lenses are introduced and the performance of systems of multiple axicons is analysed. A particular compact design that creates a ring pattern with conveniently adjustable size and sharp inner wall was modelled and realized.

The second part presents the development of a versatile control software for the DMD that allows for synchronization of the DMD with the experiment cycles and enables the projection of different dynamic sequences. An optical setup that images the DMD array directly onto the atomic ensemble was realized.

The combined setup will enable the manipulation of the quantum gas in particular ways which will allow pursuing a number of different experiments. A hard-walled box with potential adjustment in the interior will be used to create a 2D gas with uniform density. Dynamic potentials can be used to prepare non-equilibrium states, and flattening the axial trap potential for 1D systems will enable the measurement of rapidity for experimental tests of the theory of generalized hydrodynamics.

Zusammenfassung

Im Zuge dieser Arbeit wurde ein optisches System entworfen und realisiert, das ein durch Axicon-Linsen erzeugtes, einstellbares Ringmuster mit maßgeschneiderten Lichtmustern, erzeugt von einem digitalen micromirror-device (DMD) kombiniert. Dieses System wird in ein Experiment mit kaltem ^6Li Quantengas integriert werden.

Im ersten Teil werden verbesserte Ray-Tracing-Matrizen für Axicon-Linsen vorgestellt und das Verhalten von Systemen mit mehreren Axicons analysiert. Ein spezielles, kompaktes Design, das ein Ringmuster mit bequem einstellbarer Größe und scharfer Innenwand erzeugt, wird modelliert und realisiert.

Der zweite Teil präsentiert die Entwicklung einer vielseitigen Steuerungssoftware für das DMD, die eine Synchronisation des DMD mit den Experiment-Zyklen erlaubt und die Projektion verschiedener dynamischer Sequenzen ermöglicht. Ein optischer Aufbau, der das DMD-Array direkt auf das atomare Ensemble abbildet, wurde realisiert.

Der kombinierte Aufbau wird die Manipulation des Quantengases auf spezifische Weise ermöglichen, sodass eine Reihe verschiedener Experimente durchgeführt werden kann. Eine Box mit harten Wänden und einer Potenzialanpassung im Inneren wird verwendet werden, um ein 2D-Gas mit einheitlicher Dichte zu erzeugen. Dynamische Potenziale können zur Herstellung von Nichtgleichgewichtszuständen verwendet werden, und die Abflachung des axialen Fallenpotenzials für 1D-Systeme wird die Messung der Rapidität für experimentelle Tests der Theorie der verallgemeinerten Hydrodynamik ermöglichen.



Die approbierte gedruckte Originalversion dieser Diplomarbeit ist an der TU Wien Bibliothek verfügbar
The approved original version of this thesis is available in print at TU Wien Bibliothek.

Contents

1. Introduction	1
1.1. The lithium experiment	1
1.2. AC Stark shift	2
1.3. Objectives	4
2. Hard-wall ring potential	5
2.1. The Axicon	6
2.1.1. Ray Transfer matrix of the axicon	9
2.1.2. Using one axicon for trapping atoms	16
2.2. 3-axicon design for forming a tunable ring image	18
2.2.1. Creation of the first intermediate ring image	19
2.2.2. The Axicon Pair - setting the ring size	20
2.2.3. Pattern projection	26
2.3. Experimental Setup	28
2.3.1. Cage system and Layout	30
2.3.2. Setting the ring size	30
2.3.3. Light sources	32
2.3.4. Test setup and Results	32
2.3.5. Technical details	34
3. Creation of tailored and dynamic potentials	39
3.1. Digital micro mirror device	40
3.1.1. ViALUX V-9001c	40
3.2. Optical setup	41
3.2.1. Test setup	44
3.3. DMD operation and control program	44
3.3.1. Introduction to the ALP-4.3 API	44
3.3.2. Device capabilities and modes of operation	47
3.3.3. General Program structure	50
3.3.4. Modes of operation	52
3.3.4.1. Continuous display mode	53
3.3.4.2. Self-triggered mode	53
3.3.4.3. Externally-triggered mode	54
3.3.5. Graphical User Interface	57
3.4. The combined axicon and DMD setup	59
4. Conclusion and Outlook	63

Bibliography	i
A. Ring patterns produced by the axicon setup	vii
B. Flowcharts of externally-triggered mode	ix

1. Introduction

Ultracold gases [1] in low dimensions provide a unique platform to study strongly interacting quantum many-body systems. ${}^6\text{Li}$ is especially suited for this, because its broad Feshbach resonance [2] makes it possible to tune interactions from weakly attractive to strongly repulsive. This allows for both accessing the BCS regime, where atoms form cooper pairs as well as the BEC regime, where the atoms form bosonic ${}^6\text{Li}_2$ molecules [3–6].

When studying ultra-cold quantum gases of bosons, fermions or molecules, traditionally the gases are trapped in a harmonic trapping potential. This leads to an inhomogeneous density distribution which brings certain disadvantages, like a more complicated theoretical description. Furthermore the trap geometry is fixed, which limits the types of experiments that can be performed.

To study non-equilibrium systems, by performing quenches and exerting dynamic control over the atoms, as well as preparing gases in special trap geometries, calls for the creation of tailored and dynamic potential landscapes for the atomic ensemble.

1.1. The lithium experiment

This thesis was written in the context of a ${}^6\text{Li}$ cold quantum gas experiment that is designed to study a variety of physical phenomena, with a focus on out-of-equilibrium physics in strongly interacting many-body systems. A detailed description of the system is given by Liang [7] in his PhD thesis.

As a first step ${}^6\text{Li}$ metal is heated in an oven. This provides a gas of lithium atoms, which is then laser cooled with a Zeman-slower. Next the atoms reach a first chamber where they are trapped in an magneto-optical trap (MOT). The atoms are transferred directly from the MOT into an optical dipole trap. A second optical dipole trap (transport beam) then takes over the atoms. Changing the curvature of a liquid lens shifts the focus of the beam from the MOT chamber to the science cell. The atoms follow the focus of the beam, which transports them to the science cell. Here the atoms are captured by another optical dipole trap (capture trap). Before and after the transport evaporative cooling is performed, cooling the atoms to quantum degeneracy. Outside the science cell a pair of coils can be used to create a magnetic field, which allows for tuning the scattering length and thus the interaction strength, by using a Feshbach resonance. In the science chamber the atoms currently are confined in the capture trap, in the future the atom cloud will be loaded into optical lattices to create either a single 2D layer of gas, or several

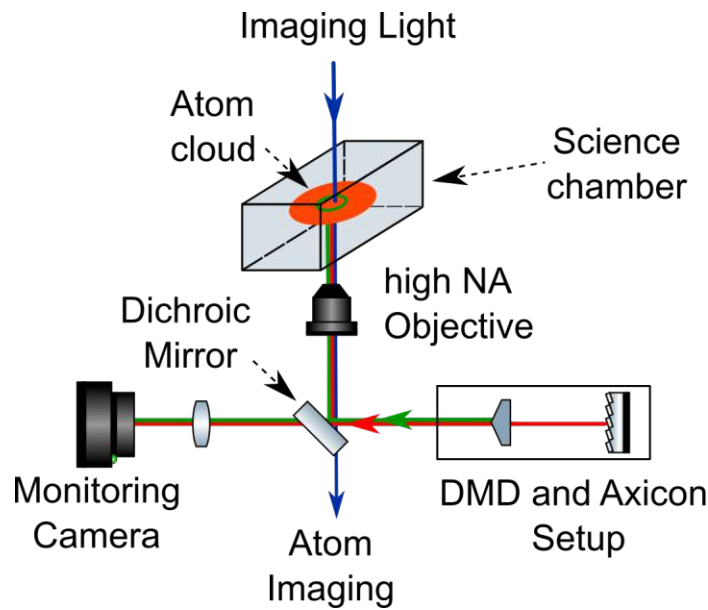


Figure 1.1.: Location of the setup below the science chamber: The new setup uses the high-NA objective to project a light potential onto the atom cloud from below.

1D tubes. The atoms are imaged via a high-NA objective that is located directly beneath the science cell. After performing an experiment and taking an image as a measurement, the process of cooling, trapping and transferring atoms start anew, with each experimental cycle taking about 15 seconds.

1.2. AC Stark shift

Trapping the atoms in the science cell utilizes the interaction between light of spatially varying intensity and a dipole that is induced in the atoms by the light. Projecting light with a certain intensity profile results in a potential landscape for the atoms. To get a good understanding of this phenomenon this section closely follows a semi-classical derivation as given in the review of by Grimm et al. [8].

In the semi-classical picture, if an atom is placed in a monochromatic light field a dipole moment \mathbf{p} is induced that oscillates with the frequency ω of the electric field $\mathbf{E}(\mathbf{r}, t)$. The amplitudes of the dipole moment and the electric field are related by the *complex polarizability* α :

$$\mathbf{p} = \alpha(\omega)\mathbf{E}. \quad (1.1)$$

The real and imaginary part of α describe the in- and out-of-phase component of the dipole oscillation. The real part $\Re(\alpha)$ is responsible for the dispersive

properties, the imaginary part $\Im(\alpha)$ describes absorption. This can be seen in the interaction potential U_{dip} and the scattering rate Γ_{sc} :

$$U_{dip}(\mathbf{r}) = -\frac{1}{2}\langle\mathbf{p}(\mathbf{r},t)\mathbf{E}(\mathbf{r},t)\rangle = -\frac{1}{2\epsilon_0c}\Re(\alpha)I(\mathbf{r}) \quad (1.2)$$

$$\Gamma_{sc}(\mathbf{r}) = \frac{\langle\dot{\mathbf{p}}(\mathbf{r},t)\mathbf{E}(\mathbf{r},t)\rangle}{\hbar\omega} = \frac{1}{\hbar\epsilon_0c}\Im(\alpha)I(\mathbf{r}), \quad (1.3)$$

where $I = 2\epsilon_0c|E|^2$, the angled brackets denote the time average over the oscillating terms and the factor $1/2$ takes into account that the dipole moment is induced and not permanent. To calculate α a semiclassical approach can be used. The atom is considered as a two-level quantum system interacting with the classical radiation field, with a resonance frequency ω_0 . The damping rate is determined by the dipole matrix element between ground state $|g\rangle$ and excited state $|e\rangle$,

$$\Gamma = \frac{\omega_0^3}{3\pi\epsilon_0\hbar c^3}|\langle e|\mu|g\rangle|^2, \quad (1.4)$$

with μ representing the electric dipole operator [8]. The explicit expressions for the dipole potential and the scattering rate in the relevant case of large detuning $\Delta = \omega - \omega_0$ and negligible saturation are:

$$U_{dip}(\mathbf{r}) = -\frac{3\pi c^2}{2\omega_0^3}\left(\frac{\Gamma}{\omega_0 - \omega} + \frac{\Gamma}{\omega_0 + \omega}\right)I(\mathbf{r}), \quad (1.5)$$

$$\Gamma_{sc}(\mathbf{r}) = \frac{3\pi c^2}{2\hbar\omega_0^3}\left(\frac{\omega}{\omega_0}\right)^3\left(\frac{\Gamma}{\omega_0 - \omega} + \frac{\Gamma}{\omega_0 + \omega}\right)^2I(\mathbf{r}). \quad (1.6)$$

These expressions show an additional so-called counter-rotating resonance at $\omega = -\omega_0$, that can be neglected in the relevant case of $|\Delta \ll \omega_0|$ (rotating-wave approximation) and set $\omega/\omega_0 \approx 1$. This simplifies equations 1.5 and 1.6 to:

$$U_{dip}(\mathbf{r}) = \frac{3\pi c^2}{2\omega_0^3}\frac{\Gamma}{\Delta}I(\mathbf{r}), \quad (1.7)$$

$$\Gamma_{sc}(\mathbf{r}) = \frac{3\pi c^2}{2\hbar\omega_0^3}\left(\frac{\Gamma}{\Delta}\right)^2I(\mathbf{r}). \quad (1.8)$$

Inspecting these two equations highlights two important factors for creating a dipole potential:

- *Sign of detuning*: Depending on the sign of the detuning Γ there exist two regimes:
 - $\Gamma < 0$ - *red detuned*: The dipole potential is negative, the interaction attracts the atoms into the light field.

- $\Gamma > 0$ - *blue detuned*: The dipole potential is positive, the interaction repels the atoms out of the light field.
- *Scaling with I and Δ* : The dipole potential scales with I/Δ , where as the scattering rate scales with I/Δ^2 . This means large detunings and high intensities can be used to keep the scattering rate low at a given potential depth.

A more detailed calculation from first principles of the ac polarizability of lithium was performed by Safronova et al. [9]. The values for the wavelengths relevant for this thesis are given in table 1.1. The conversion from atomic units to SI-units

λ [nm]	α [a.u.]	$\alpha_{SI}[Jm^2/W]$
520	-288 a.u.	$-8.9 \cdot 10^{-37}$
641	-1643 a.u.	$-5.08 \cdot 10^{-36}$

Table 1.1.: AC polarizabilities of ${}^6\text{Li}$ by Safronova et al.[9]

was performed by multiplying by $e^2 a_0^2 / E_h$, where e is the electron charge, a_0 is the Bohr radius and $E_h = \hbar^2 / (m_e a_0^2)$ is the Hartree energy. Since Safronova et al. uses a different notation $U = \alpha I$ also the factor $\frac{1}{2\epsilon_0 c}$ out of equation 1.2 has to be taken into account.

1.3. Objectives

As previously stated, the creation of tailored and dynamic optical potentials is needed to study various non-equilibrium phenomena. Some specific topics we aim to investigate with the Lithium experiment include tests of the theory of generalized hydrodynamics (GHD) in 1D systems and the study of vortices and phase transitions in 2D. For study of 2D phenomena a system with homogeneous density is needed, which can be realized with a 2D box potential as the trapping potential. To create this, one needs to confine the atoms in the xy-direction by a steep wall and shape the interior of the trap to have a flat bottom.

Recently digital micro mirror devices have been implemented into cold atom experiments to shape the trapping potential and realize dynamic and tailored traps, including box traps [10, 11]. Additionally a system of axicons has been utilized to create a ring shaped wall potential for a 2D trap in a cold atoms experiment [11]. The goal of this diploma project is to design and realize a system, that uses both a DMD and an axicon setup. This combined setup will be placed below the science cell and will project patterns onto the atoms from below through the high-NA objective (see figure 1.1).

2. Hard-wall ring potential

When designing a system for confining atoms into a box potential there are several requirements for the properties of the walls of the box:

- The walls should be as steep as possible, ideally only limited by the diffraction limit.
- The interior of the trap should be left as dark as possible.
- The size of the trap should be easily changeable, without swapping out components. Rings sizes should cover a range of $\sim 20 - 200 \mu\text{m}$.
- The power consumption of the system should be small, to avoid the need for high powered lasers, possibly below 100 mW.
- The system should be small in order to save space in the experiment (optical pathlength $< 1000 \text{ mm}$).
- The setup needs to project the potential onto the atoms using the existing infinity corrected high-NA objective.

There are several ways of meeting these requirements. One would be to use a digital micro-mirror device (DMD) or a spacial light modulator (SLM). Both those approaches come with their own difficulties and both are more costly and complicated solutions. Here a different approach was chosen: Utilizing conical lenses, called axicons, allows for the creation of a ring-shaped wall potential [12]. Such a setup enables the creation of a ring potential with changeable size, while also having high power efficiency and being relatively simple compared to more complicated active devices as SLMs/DMDs. The strengths of a DMD lie elsewhere, which utilized in chapter 3.

It has been shown that a axicon can be used to trap atoms in a repulsive ring potential [13]. In his dissertation, Hueck [11] implemented a more complicated axicon setup using several axicons. A similar system had been implemented before for trapping biological samples [14].

Following this approach, I further investigated the properties of such a setup for our application, while finding a system design that meets the special requirements. The aim of this chapter is to collect all the necessary knowledge on using axicons for trapping atoms and provide analysis and explanation on how axicon lenses work. I introduce an improved ray tracing matrix and examine analytical ray tracing, to enable accurate simulations of the axicon's behavior. Furthermore I present the capabilities of the system that was implemented in the setup and

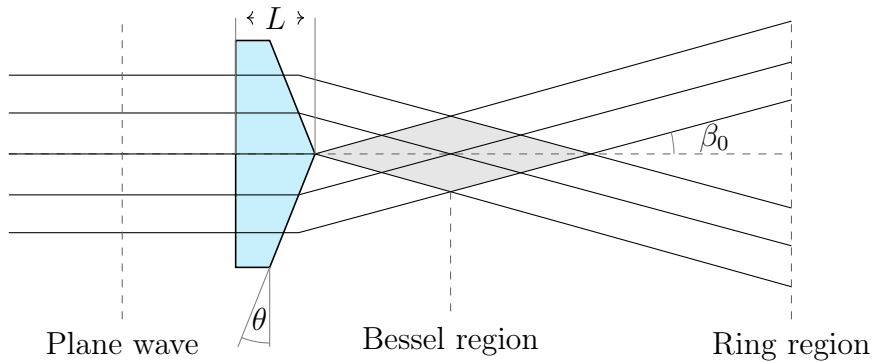


Figure 2.1.: Basic working principle of the axicon: An impinging plane wave gets diffracted by the axicon, the beams overlap and create a Bessel region. In the far field a ring is formed.

comprehensively outline the design concepts, point out difficulties and problems that one may encounter during its design and setup.

2.1. The Axicon

The term ‘axicon’ was originally introduced to refer to a broad group of optical components that are all figures of revolution [12]. Today it commonly refers to the conical, refractive axicon, sometimes also called ‘conical lens’, that consists of one flat surface and one shaped like a cone, and is illuminated along the axis of rotation (figure 2.1).

An axicon is characterized by its thickness L , refractive index n , and base angle θ , also called its axicon angle (see figure 2.1). When a plane wave impinges on the axicon, the refracted parts of the beam first interfere with each other and create a Bessel-like beam. After this diffraction zone, a clean, ring-shaped beam is created, that diverges with an angle β_0 .

Both the axicon’s near- and far field properties have been used in many applications like Laser drilling [15], trapping of biological samples [14], alignment of optical systems and mechanical devices, testing the flatness of large surfaces, detecting small objects by observing scattered light and optical triangulation [16]. For the purpose of this thesis we will focus on the ring-shaped beam in the far-field, that will be used as the hard wall of the box potential.

In the case of a plane wave impinging on the axicon (figure 2.1) the ring-shaped crosssection along the diverging beam shows sharp edges and uniform intensity along the walls. The diverging angle of the beam can be calculated with Snell’s

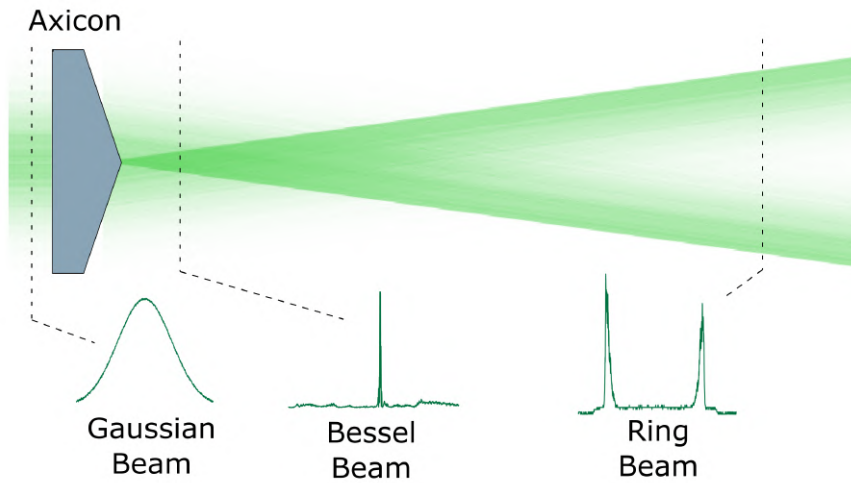


Figure 2.2.: Simulation of a Gaussian beam interacting with an axicon: Within the Bessel region the cross section of the beam is a Bessel beam. Further away a ring is formed which has steep outer edges.

law and is given by:

$$\beta_0 = \arcsin(n \cdot \sin \theta) - \theta \quad (2.1)$$

In a more realistic setting the input light would be a laser beam with Gaussian intensity distribution instead of a plane wave with uniform intensity. Additionally the tip of the axicon is not perfectly sharp, but has a finite bluntness. As shown in figure 2.2, this leads to a Bessel beam being formed in the diffraction region as well as to a more complex structure of the ring-shaped beam profile in the far-field. The ring pattern has a sharper outer edge than the inner one. The intensity profile of the inner edge also shows intensity variations, which can be attributed to imperfections of the optical surface around the axicon's tip [15].

Equation 2.1 assumes rays that are perpendicular to the flat surface of the axicon. A more general expression for the angle β after the axicon can be derived for the situation depicted in figure 2.3, when the incoming ray is tilted by an angle α , which can take values between $-\frac{\pi}{2}$ and $+\frac{\pi}{2}$.

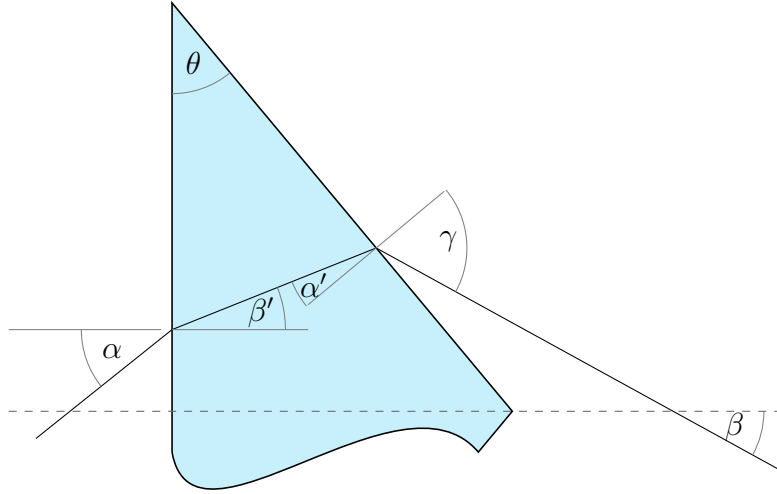


Figure 2.3.: Angles for a ray traveling through the upper half plane of an axicon

Snells' law can be applied at both surfaces of the axicon

$$\sin \alpha = n \cdot \sin \beta' \implies \beta' = \arcsin \left(\frac{\sin \alpha}{n} \right) \quad (2.2)$$

$$\sin \gamma = n \cdot \sin \alpha' \quad (2.3)$$

Furthermore, as shown in figure 2.3, the following angle relations can be derived:

$$\alpha' = \theta - \beta' \quad (2.4)$$

$$\beta = \gamma - \theta \quad (2.5)$$

Inserting Eq. 2.4 into 2.3 gives:

$$\sin \gamma = n \cdot \sin(\theta - \beta') = n \cdot (\sin \theta \cdot \cos \beta' - \sin \beta' \cdot \cos \theta) \quad (2.6)$$

Here the identity $\sin(a - b) = (\sin a \cdot \cos b - \sin b \cdot \cos a)$ was used.

Inserting equation 2.2 results in:

$$\sin \gamma = n \cdot \sin \theta \cdot \cos \left(\arcsin \left(\frac{\sin \alpha}{n} \right) \right) - \sin \alpha \cdot \cos \theta \quad (2.7)$$

This can be rewritten by using $\cos(\arcsin x) = \sqrt{1 - x^2}$. The positive sign in front of the square root is ensured by the definition of arcsin-function, which can only take values between $-\frac{\pi}{2}$ and $+\frac{\pi}{2}$:

$$\gamma = \arcsin \left[n \cdot \sin \theta \cdot \sqrt{1 - \frac{\sin^2 \alpha}{n^2}} - \sin \alpha \cdot \cos \theta \right] \quad (2.8)$$

Using equation 2.5 leads to the final result for the angle β after the axicon, if a ray with angle α impinges on an axicon with base angle θ and refractive index n :

$$\beta(\alpha) = \arcsin \left[\mp n \cdot \sin \theta \cdot \sqrt{1 - \frac{\sin^2 \alpha}{n^2}} - \sin \alpha \cdot \cos \theta \right] \mp \theta \quad (2.9)$$

The derivation was done for the upper half plane, denoted by the upper sign in the formula. A similar derivation gives the result for the lower half plane denoted by the lower signs. Inserting $\alpha = 0$ gives the same result as equation 2.1. Having derived the exact result, in the next section ray transfer matrices will be used to numerically simulate axicons.

2.1.1. Ray Transfer matrix of the axicon

Ray transfer matrix analysis uses matrices to calculate the effect of optical components on rays of light. It uses the small angle approximation, so it is only valid for paraxial rays [17]. In a 2D plane that includes the optical axis, a ray is represented by an vector $(y, \alpha)^T$, where y represents the distance from the optical axis and α the angle between the ray and the optical axis. An optical component is represented by a 2×2 -matrix and its effect on a ray can be calculated by multiplying the ray vector with the matrix:

$$\begin{pmatrix} y_2 \\ \beta \end{pmatrix} = \begin{pmatrix} A & B \\ C & D \end{pmatrix} \cdot \begin{pmatrix} y \\ \alpha \end{pmatrix}, \quad (2.10)$$

where y_2 is the new height and β the new angle of the ray after the axicon. This relation is depicted in figure 2.4a. The transfer matrices M_T of a propagation through free space over a distance d and M_L for a thin lens with focal length f are:

$$M_T = \begin{pmatrix} 1 & d \\ 0 & 1 \end{pmatrix}, M_L = \begin{pmatrix} 1 & 0 \\ -\frac{1}{f} & 1 \end{pmatrix} \quad (2.11)$$

2×2 -matrices can only describe simple components [17]. For components like the axicon, a 3×3 -matrix is needed. The special 3×3 -matrix shown in equation 2.12 describes an additional decentering v and tilting φ [17], as shown in figure 2.4b. Using 3×3 -matrices also adds an additional row to the vectors describing the rays which is just set to 1. The equation for calculating the vector after an optical component changes to

$$\begin{pmatrix} y_2 \\ \beta \\ 1 \end{pmatrix} = \begin{pmatrix} A & B & v \\ C & D & \varphi \\ 0 & 0 & 1 \end{pmatrix} \cdot \begin{pmatrix} y \\ \alpha \\ 1 \end{pmatrix}. \quad (2.12)$$

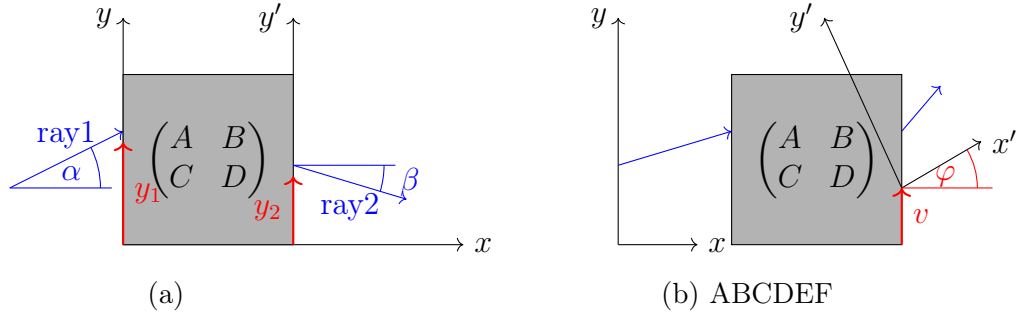


Figure 2.4.: Schematic comparison of the working principle of a 2×2 -ray transfer matrix (a) and a 3×3 -ray transfer matrix (b). The 3×3 -matrix introduces additional tilt and decentering compared to the 2×2 case.

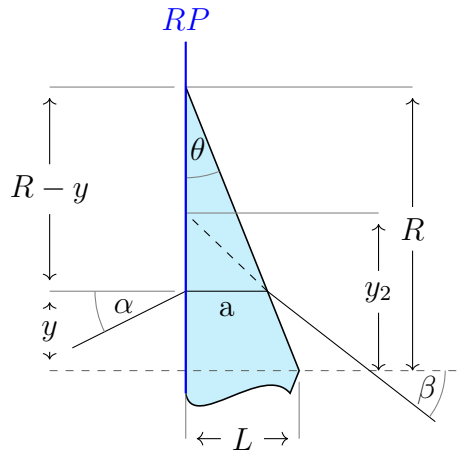


Figure 2.5.: Simplified schematic depiction of a ray travelling through the upper half of an axicon

The ray transfer matrix of the axicon was first given by Zhao [18]. Its validity is based on several assumptions:

- A ray exits the axicon at the same height as it enters.
- The axicon bends each ray by the same angle $\beta = \alpha \mp \beta_0$, regardless of how big angle α of the impinging ray is.
- The bending angle β_0 is calculated with equation 2.1.

These assumptions hold for small angles α , as will be shown later. Figure 2.5 shows a ray passing through the axicon under this small-angle approximation, enabling the derivation of a relationship between the depicted quantities. Note that the following derivation applies to the upper half plane, while a similar derivation can be done for the lower half plane. The flat side of the axicon is chosen as a reference plane (labeled RP in figure 2.5). It is assumed that the incoming ray hits RP at height y with angle α and then continues after the RP from height y_2 and angle β . The following relations can be derived:

$$R = \frac{L}{\tan \theta} \quad (2.13)$$

$$a = (R - y) \cdot \tan \theta = \left(\frac{L}{\tan \theta} - y \right) \cdot \tan \theta = L - y \cdot \tan \theta \quad (2.14)$$

$$\begin{aligned} y_2 &= y + a \cdot \tan \beta = y + (L - y \cdot \tan \theta) \cdot \tan \beta = \\ &= (1 - \tan \beta \cdot \tan \theta) \cdot y + L \cdot \tan \beta \end{aligned} \quad (2.15)$$

This, together with $\beta = \alpha + \beta_0$, leads to the ray transfer matrix of the axicon as given by [18]:

$$M_{ax} = \begin{pmatrix} 1 - \tan \theta \cdot \tan \beta_0 & 0 & \pm L \cdot \tan \beta_0 \\ 0 & 1 & \mp \beta_0 \\ 0 & 0 & 1 \end{pmatrix}, \quad (2.16)$$

where L is the thickness of the axicon, θ is the base angle of the axicon and β_0 is the bending angle calculated with equation 2.1. The upper signs refer to the upper half plane of the axicon.

The approximations used in this derivation resemble the thin lens approximation for spherical lenses. For more accurately calculating the axicon's behavior next we want to investigate if there is a more complete linear approximation that can be written in matrix form.

To achieve this, an analytical solution for the ray vectors $(y_2, \alpha_2)^T$ after the axicon is derived, expanded for small angles α and then compared to the matrix in equation 2.16. Furthermore a new axicon matrix for an axicon pointing in the opposite direction (tip facing the incoming light) is derived.

From analytical solution to ray-tracing matrices

Axicon in forward orientation: >

First consider the forward-facing axicon, where the flat surface is oriented towards the incoming light. The derivation for the upper half plane is presented here, the derivation for the lower half plane can be obtained following the same procedure, or by substituting the axicon angle θ with $-\theta$ in the solution for the upper half plane. Again the flat surface of the axicon is chosen as a reference plane.

The analytical solution for the angle after the axicon β is given by equation 2.9. Since the transfer matrix only can hold terms that are linear in α and y , equation 2.9 is Taylor-expanded and only the linear terms are considered. It is assumed that $|\alpha|$ is small and thus the expansion is centered around $\alpha = 0$:

$$\beta(\alpha) = \beta(0) + \left. \frac{\partial \beta}{\partial \alpha} \right|_{\alpha=0} \alpha + \left. \frac{\partial^2 \beta}{\partial \alpha^2} \right|_{\alpha=0} \frac{\alpha^2}{2} + \mathcal{O}(\alpha^3) \quad (2.17)$$

$$= \theta - \arcsin(n \sin(\theta)) + \frac{\alpha \cos(\theta)}{\sqrt{1 - n^2 \sin^2(\theta)}} + \mathcal{O}(\alpha^2) \quad (2.18)$$

$$= -\beta_0 + \alpha \frac{\cos(\theta)}{\sqrt{1 - n^2 \sin^2(\theta)}} + \mathcal{O}(\alpha^2) \quad (2.19)$$

The first term corresponds to $\beta(0)$ (see equation 2.1).

The analytical solution for the ray height y can be derived as:

$$y_2 = y + \frac{L - \tan \theta}{1 - \tan \theta \tan(\arcsin(\frac{\sin \alpha}{n}))} \left(\tan \left(\arcsin \left(\frac{\sin \alpha}{n} \right) \right) - \tan \beta \right) \quad (2.20)$$

An similar expansion can be done here:

$$y_2 = y_2^{(0)} + \alpha y_2^{(1)} + \mathcal{O}(\alpha^2) \quad (2.21)$$

$$\begin{aligned} y_2^{(0)} &= y - \tan(\theta - \arcsin(n \sin(\theta))) (L - y \tan(\theta)) = y + \tan \beta_0 (L - y \tan \theta) \\ &= y(1 - \tan \beta_0 \tan \theta) + L \tan \beta_0 \end{aligned} \quad (2.22)$$

$$\begin{aligned} y_2^{(1)} &= -(L - y \tan(\theta)) \left(\frac{\cos(\theta)}{\sqrt{1 - n^2 \sin^2(\theta)}} - \frac{1}{n} + \right. \\ &\quad \left. + \frac{\tan(\theta - \arcsin(n \sin(\theta)))^2 \cos(\theta)}{\sqrt{1 - n^2 \sin^2(\theta)}} + \frac{\tan(\theta - \arcsin(n \sin(\theta))) \tan(\theta)}{n} \right) \end{aligned} \quad (2.23)$$

Since the matrix can not account for mixed terms like $\alpha \cdot y$, those are left out, which gives the first order term for the ray height:

$$y_2^{(1*)} = -\alpha L \left(\frac{\cos(\theta) (1 + \tan^2 \beta_0)}{\sqrt{1 - n^2 \sin^2(\theta)}} - \frac{1 + \tan \beta_0 \tan \theta}{n} \right) \quad (2.24)$$

The same derivation can be done for the lower half plane. Finally the first order approximation for angle β as well as the terms $y_2^{(0)}$ and $y_2^{(1*)}$ are obtained, which gives the first order ray transfer matrix for the forward facing axicon:

$$M_{ax}^{\rightarrow} = \begin{pmatrix} 1 - \tan \beta_0 \tan \theta & -L \left(\frac{\cos(\theta)(1 + \tan^2 \beta_0)}{\sqrt{1 - n^2 \sin^2(\theta)}} - \frac{1 \pm \tan \beta_0 \tan \theta}{n} \right) & \pm L \tan \beta_0 \\ 0 & \frac{\cos(\theta)}{\sqrt{1 - n^2 \sin^2(\theta)}} & \mp \beta_0 \\ 0 & 0 & 1 \end{pmatrix} \quad (2.25)$$

Comparing this new axicon matrix with the matrix in equation 2.16, it is obvious that they are similar, but the first order terms in matrix 2.25 give different terms in the second column. For small angles α and a refractive index n close to 1 the simpler matrix still gives a good approximation. It can be thought of as a “zeroth order” approximation.

Axicon in reverse orientation: <

The ray transfer matrix for an axicon facing in the opposite direction (tip towards the impinging light, see figure 2.6) has to my knowledge not been shown before. It is derived following the same steps as for the matrix for the forward facing axicon. The angle after the axicon β can be written as:

$$\beta(\alpha) = -\arcsin \left(n \sin \left(\theta - \arcsin \left(\frac{\sin(\alpha + \theta)}{n} \right) \right) \right). \quad (2.26)$$

This expression again can be Taylor-expanded which leads to:

$$\begin{aligned} \beta &\approx \frac{\alpha \cos \left(\theta - \arcsin \left(\frac{\sin(\theta)}{n} \right) \right) \cos(\theta)}{\sqrt{1 - n^2 \sin^2 \left(\theta - \arcsin \left(\frac{\sin(\theta)}{n} \right) \right)^2} \sqrt{1 - \frac{\sin^2(\theta)}{n^2}}} - \\ &\quad \arcsin \left(n \sin \left(\theta - \arcsin \left(\frac{\sin(\theta)}{n} \right) \right) \right) \\ &= \alpha \frac{\cos \beta'_0}{\sqrt{1 - n^2 \sin^2 \beta'_0}} \frac{\cos \theta}{\sqrt{1 - \frac{\sin^2 \theta}{n^2}}} - \beta_0, \end{aligned} \quad (2.27)$$

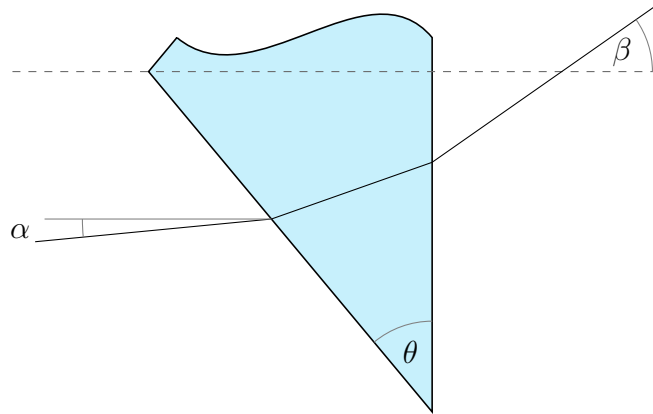


Figure 2.6.: Ray traveling through an axicon in reverse orientation

with

$$\beta_0 = \arcsin \left(n \sin \left(\theta - \arcsin \left(\frac{\sin \theta}{n} \right) \right) \right) = \arcsin (n \sin \beta'_0), \quad (2.28)$$

$$\beta'_0 = \theta - \arcsin \left(\frac{\sin \theta}{n} \right) \quad (2.29)$$

and

$$\tilde{n} = \frac{\cos \theta}{\sqrt{1 - \frac{\sin^2 \theta}{n^2}}}. \quad (2.30)$$

Note that here β_0 is calculated differently than for the other axicon orientation.

The analytical expansion for the ray height y_2 can be derived as:

$$y_2 = y - \left(L - \frac{y - L \tan \alpha}{\tan(\pi/2 - \theta) - \tan \alpha} \right) \left(\tan \alpha + \tan \left(\arcsin \frac{\sin(\alpha + \theta)}{n} \right) \right) \quad (2.31)$$

This again can be Taylor expanded and leads to:

$$\begin{aligned}
 y_2^{(0)} &= y - \tan\left(\theta - \arcsin\left(\frac{\sin(\theta)}{n}\right)\right) \left(L + \frac{y}{\tan\left(\theta - \frac{\pi}{2}\right)}\right) = \\
 &= y(1 + \tan\beta'_0 \tan\theta) - L \tan\beta'_0
 \end{aligned} \tag{2.32}$$

$$\begin{aligned}
 y_2^{(1*)} &= \alpha \left(L \left(\frac{\cos(\theta)}{n \sqrt{1 - \frac{\sin(\theta)^2}{n^2}}} + \frac{\tan\left(\theta - \arcsin\left(\frac{\sin(\theta)}{n}\right)\right)^2 \cos(\theta)}{n \sqrt{1 - \frac{\sin(\theta)^2}{n^2}}} \right) \right. \\
 &\quad \left. - L + \frac{L \tan\left(\theta - \arcsin\left(\frac{\sin(\theta)}{n}\right)\right)}{\tan\left(\theta - \frac{\pi}{2}\right)} \right) = \\
 &= -\alpha L (1 + \tan\beta'_0 \tan\theta) + \alpha L (1 + \tan^2\beta'_0) \frac{\cos\theta}{n \sqrt{1 - \frac{\sin^2\theta}{n^2}}}
 \end{aligned} \tag{2.33}$$

Calculations for the lower half plane show a similar result with some changed signs. Together with the result for the upper half plane, they give the ray transfer matrix for the reverse facing axicon:

$$M_{ax}^{\leftarrow} = \begin{pmatrix} 1 + \tan\beta'_0 \tan\theta & L(1 + \tan^2\beta'_0) \frac{\tilde{n}}{n} - L(1 \pm \tan\beta'_0 \tan\theta) & \mp L \tan\beta'_0 \\ 0 & \tilde{n} \frac{\cos\beta'_0}{\sqrt{1 - n^2 \sin^2\beta'_0}} & \mp \beta_0 \\ 0 & 0 & 1 \end{pmatrix}$$

Comparison of the axicon matrices

When using ray transfer matrices in optical simulations the error of the free space propagation matrix (equation 2.11) can serve as a benchmark to which other matrices can be compared to, to give a sense of the order of magnitude of the approximation error. This free space propagation error, which comes from the approximation of $\tan\alpha$ as α is shown in figure 2.7 (purple line) together with the errors the different axicon matrices make compared to their respective exact solutions. For the ray height y_2 the relative errors and for the angle β the errors in mm after a distance of 100 mm are shown. When comparing the exact solutions (blue), 0-th order axicon matrix (black), first order approximation (yellow) and the newly derived axicon matrix (green), it is clear that the new first order matrix reduces the error made, especially for the ray height y_2 . For the angle β the new matrix reduces the error as well and brings it closer towards the purple line. For small angles, both the 'old' and 'new' matrices give good results close to the exact solution.

Since later in this work systems of several axicons will be investigated, it has to be noted that the rays after one axicon ($\theta = 10^\circ$) have an angle of $\beta_0 \approx 4.8^\circ$.

If those rays now reach a second axicon their impinging angles $\alpha = \beta_0$ can not be considered small any more, and the axicon matrices as well as the free space propagation matrix will start to give significant errors. This has to be kept in mind when calculating the ray traces of systems of several axicons. For the axicon system designed in this thesis the ray transfer matrix approach gives good enough results to understand and simulate basic properties of such a system. For more exact calculations a more precise ray tracing approach need to be considered. After understanding the function of one axicon, and having acquired a linear approximation for it, that can be used in numerical simulation, the next step is to have a look at how axicons can be used trap atoms by creating a ring potential that meets the requirements layed out in the beginning section 2.

2.1.2. Using one axicon for trapping atoms

The idea for using an axicon to trap atoms was first realized by Manek et al. [13] by simply combining an axicon with a lens, that focuses the light onto the atoms. This approach has several disadvantages. First, the sharp edges of the ring are on the outside of the circle, whereas the inner walls are not very steep. Furthermore such a simple setup is susceptible to imperfections of the axicon's tip [11, 15], which leads to stray light that reduces the darkness inside of the circle. In the past, this issues were solved by blocking out the center with a circular disc [13], but this has the disadvantage of having to exchange for a different size disk when changing the ring size.

To avoid these disadvantages, a slightly more complex design involving three axicons was designed and used to trap atoms in the Group of Henning Moritz [11]. A similar design was used previously to trap biological samples in a ring potential with variable size by Shao et al. [14]. In the next section I follow this approach, investigate it in detail and use it to design a compact system for generation of a tunable ring image.

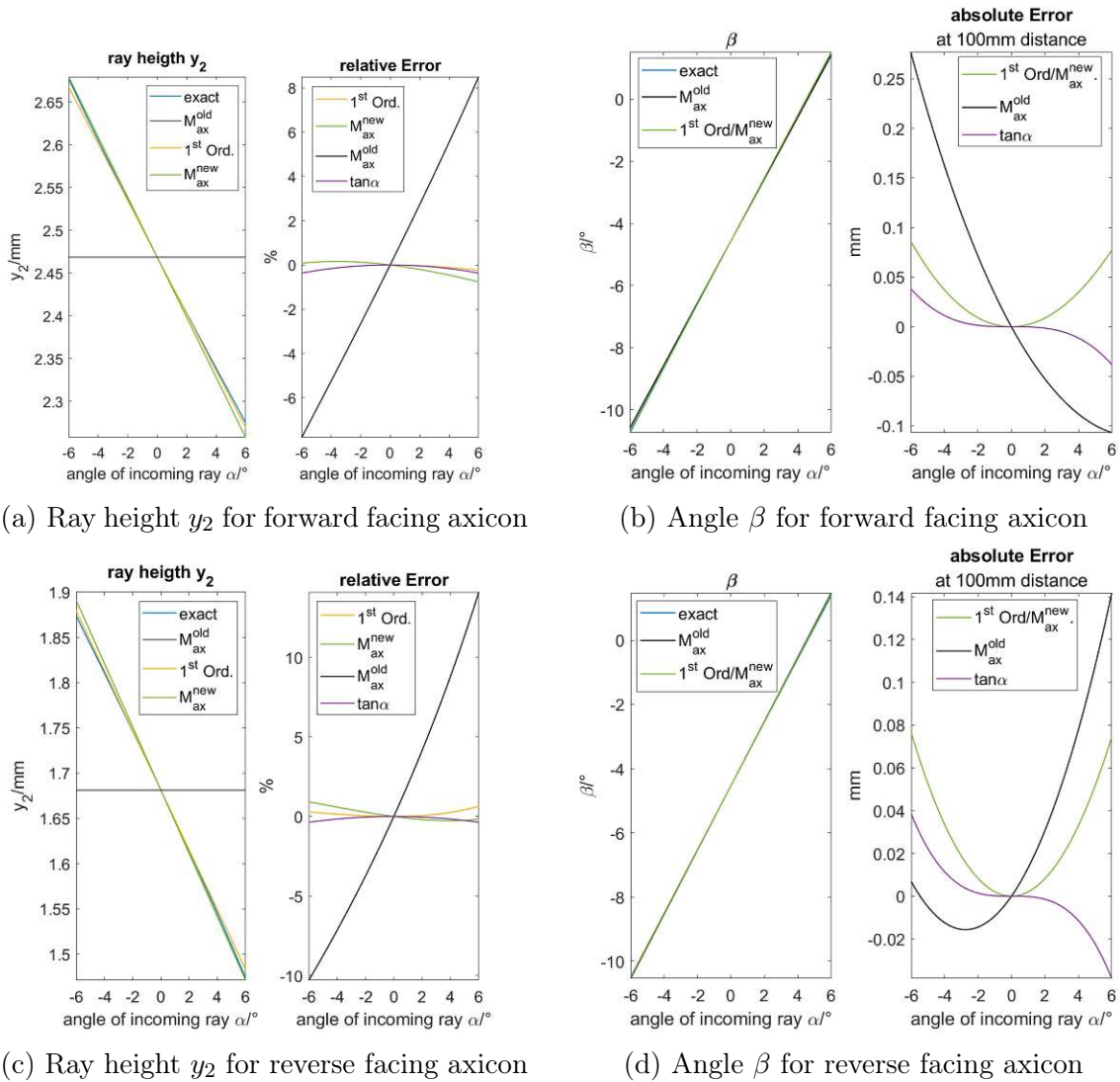


Figure 2.7.: Error of ray transfer matrices: Figures depict the values (left) and errors (right) of the ray transfer matrices of a typical axicon ($L = 6.2\text{mm}$, $\theta = 10^\circ$, $n = 1.45$). (a) and (b) show the forward facing axicon $>$, (c) and (d) the reverse facing axicon $<$. Blue lines show the exact solution, black the 0th-order axicon matrix, yellow the 1st-order approximations and green the newly derived 1st-order axicon matrix. For comparison, the purple graphs in (b) and (d) show the error made when approximating $\tan \alpha \approx \alpha$.

2.2. 3-axicon design for forming a tunable ring image

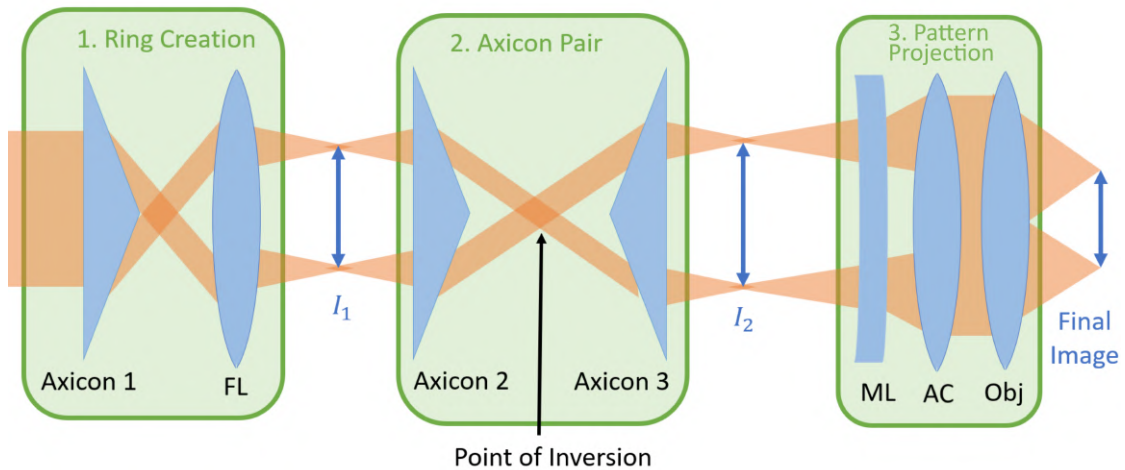


Figure 2.8.: Schematic of the 3-axicon system: 1) The first axicon creates a ring and the focusing lens (FL) causes the first intermediate image I_1 to form. 2) The axicon pair is used to invert the beam, creating sharp inner walls after the point of inversion, and to change the ring size, which creates an intermediate image I_2 . 3) The pattern is projected onto the atoms via a concave magnifying lens (ML), an achromat (AC) and an objective (Obj). The objective is a custom high-NA objective (Special Optics, design number 57-28.1-28), which is also used to image the atoms.

The system consists of 3 axicons, a focusing lens that create the ring-shaped pattern and additional lenses that project it onto the atoms (figure 2.8). To understand the functions of different parts of the system it is helpful to visualize several intermediate images that are created throughout the system. An intermediate image refers to a location along the beam where the light rays converge to form a ring-shaped image. These can be virtual or real images, depending on the position of the individual components. For simplicity the system is divided into 3 parts (see figure 2.8):

1. Ring Creation
2. Axicon Pair - Setting the ring size and creating inversion
3. Pattern projection

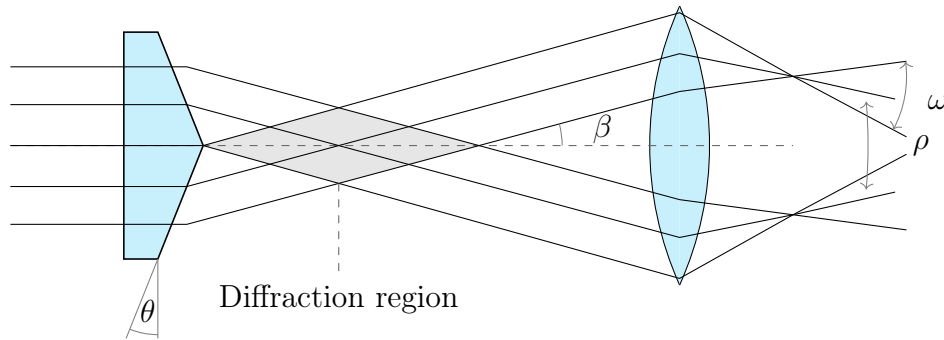


Figure 2.9.: Creation of a first intermediate image: The focusing lens focuses the ring created by the first axicon which creates an image. The wall divergence ω describes how much the walls of the ring diverge, the ring divergence ρ describes how the ring size changes along the beam, and is positive if the ring gets bigger.

The first part resembles the simple setup used by Manek et al. [13], where an axicon (axicon 1) creates a diverging ring-shaped beam and the focusing lens (FL) creates the first intermediate image I_1 . This image is then changed in size and inverted by the axicon pair (axicon 2 and 3). The use of the axicon pair allows for the creation of an intermediate image I_2 with easily changeable size and sharp inner walls. I_2 is then finally projected onto the atoms by a concave magnifying lens (ML), an achromat (AC) and a high-NA objective (obj). The objective is a custom high-NA objective (Special Optics, design number 57-28.1-28), which is also used for imaging of the atoms.

In the following detailed analyses of each part of the system are given to explain how such a system produces the hard wall ring pattern for a 2D box potential.

2.2.1. Creation of the first intermediate ring image

The first axicon converts the incoming Gaussian beam into a diverging hollow beam with a ring-shaped crosssection. Even though the whole beam is diverging, rays in a slice along the cone are still close to parallel to each other and there is no ring-shaped image formed. The focusing lens is needed to create an image, that forms at the focal plane of the lens, as is shown in figure 2.9. From here I will refer to this image as the first intermediate image I_1 .

For clarity, let's define two different divergences within the system (see figure 2.9):

- **wall divergence ω** : divergence of the rays as caused by a lens

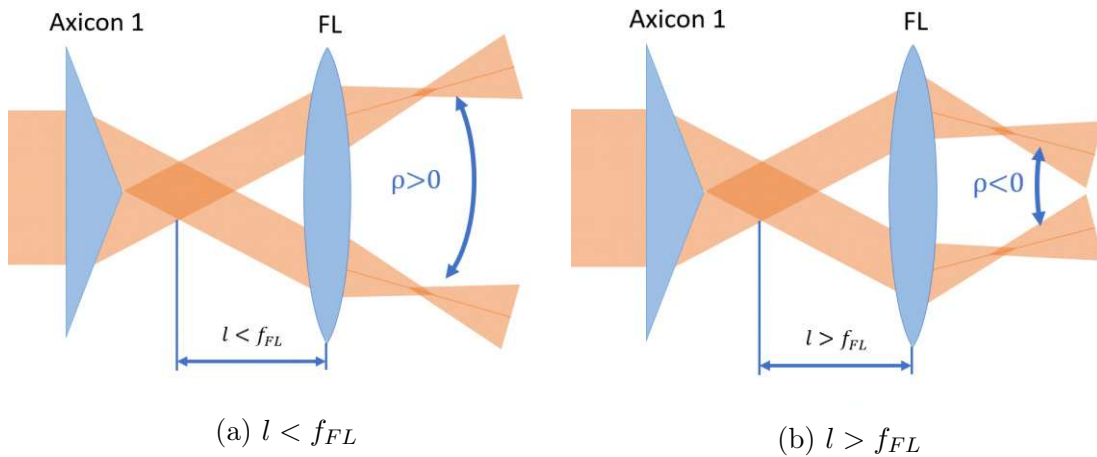


Figure 2.10.: Change of ring divergence ρ by the focusing lens: Depending on how far away from the center of the diffraction zone (dark orange) the focusing lens is placed, ρ is either positive or negative. If the distance is exactly the focal length $\rho = 0$.

- **ring divergence** ρ : divergence of the cone created by the axicon, that changes the ring size along the beam

Placing an axicon inside the beam only changes the ring divergence (in the 0th order approximation), whereas placing a focusing lens changes both the wall and ring divergence. If the lens is placed closer than its focal length f_{FL} from the center of the diffraction zone, the ring divergence will be positive (figure 2.10a). Conversely, the ring divergence will be negative if the distance from the center of the diffraction zone is greater than f_{FL} (figure 2.10b). The effect on ω depends on f_{FL} . Shorter focal length means a stronger increase in ω . After the axicon enough space is needed for the ring to form. If the lens is placed within the diffraction zone, no clean ring image will be created.

Having created the first intermediate image of the ring, next the function of the axicon pair is explained.

2.2.2. The Axicon Pair - setting the ring size

After the focusing lens creates the first intermediate image, the beam travels through the axicon pair that consists of the second and the third axicon, separated by a distance d . For simplicity consider a system of two axicons with the same angle θ that are oriented with the tips facing each other (see figure 2.12). Also ρ shall be zero before the axicon pair.

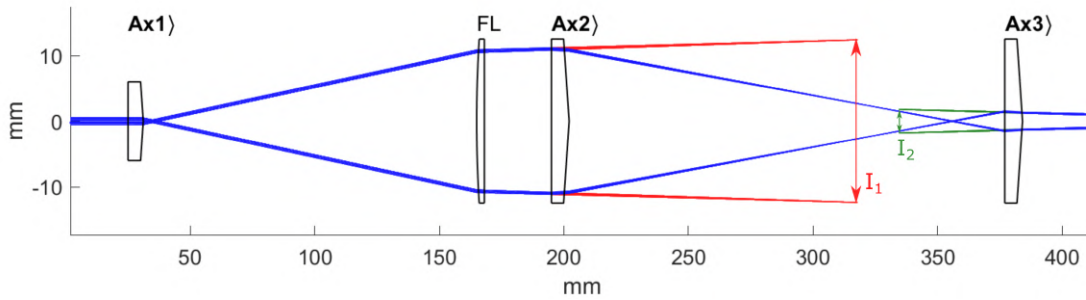


Figure 2.11.: Simulation of the first 2 parts of the 3-axicon system: The blue rays depict the path the light takes through the system and are entering from the right. The axicons are oriented with their tips pointing towards the right. Red rays form intermediate image 1, green rays intermediate image 2. Both are virtual images.

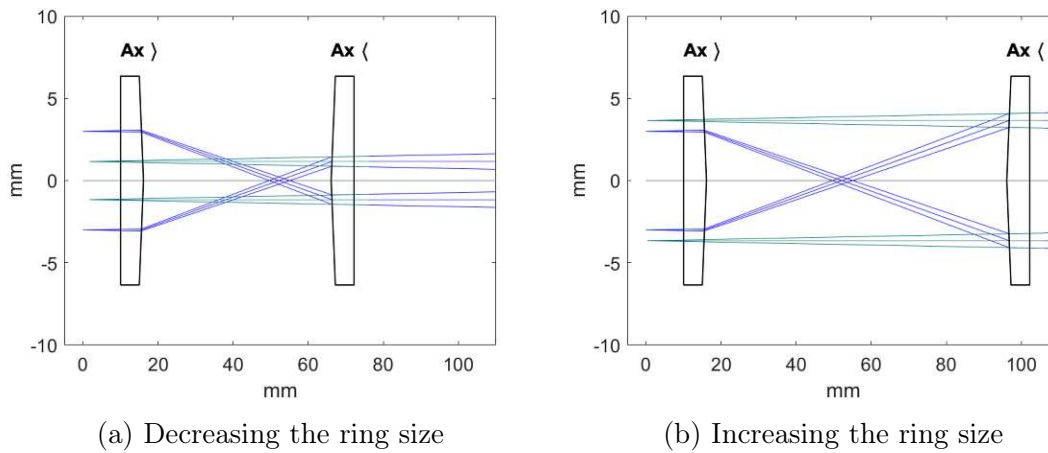


Figure 2.12.: Working principle of a pair of axicons: The ring divergence ρ is made negative by the axicon and thus the ring size gets smaller until the crossing point (point of inversion), where ρ gets positive again. The last axicon undoes the bend introduced by the former axicon. Here a virtual image (green) is created. Size and position of the virtual image depend on the distance between the two axicons.

When the rays hit the second axicon it bends the beam by β_0 , making the ring divergence $\rho < 0$. Due to this, the beam converges, inverts and diverges again. The third axicon sits after the point of inversion and undoes the bend caused by the second axicon, taking the ring divergence back to $\rho = 0$.

This has two important effects:

- *Inversion*: After the point of inversion rays that were on the outside of the ring now are on its inside. This means that the steep part of the wall profile lies on the inside of the ring, creating a sharp inner wall. This is one of the desired properties (see start of chapter 2).
- *Tuneable Size*: A second intermediate image of the ring (I_2) is created, which in this case is a virtual image. The size and position of I_2 depend on the distance d between the two axicons, which allows for changing the size of the ring that the system creates, by changing d .

The ratio of ring sizes of the intermediate images I_2/I_1 is called the *magnification* of the axicon pair.

Figure 2.12 shows how the second intermediate image (green rays) is created by the axicon pair. Note that the second intermediate image can be either a virtual or a real image, depending on where the first intermediate image is located. There are three different cases which are shown in figure 2.13:

Image	Position of Intermediate Image 1		
	before axicon pair	between axicon pair	after axicon pair
I_1	real	virtual	virtual
I_2	virtual	virtual	real

Figures 2.12 and 2.13 show that the key features of inversion and tuneable size occur regardless of if the intermediate images are virtual or real, as well as that I_2 and I_3 always have roughly the same position except for a small shift. This shift moves the image away from the focus of the following optical components and therefore should be kept small. As will be discussed in detail in the next section this shift occurs regardless of the combinations of axicons used and thus changing the ring size is always accompanied by the need to slightly reposition the other optical components to keep the image in focus.

The range of ring sizes the axicon pair can create is limited by two things:

- For large ring sizes light rays will clip on the edge of the axicon, so the **diameter** of ax3 is the limiting factor.

- For small ring sizes the tip of the third axicon needs to be brought close to the point of inversion. If this distance gets too small some light will hit the **axicon's tip**, where the finite tip radius and imperfections from manufacturing will influence the quality of the ring image created.

Avoiding the tip of the axicon is important to creating clean ring images. In a setup like shown in figure 2.13b (both I_1 and I_2 virtual images) the focus of the beam (where ω changes sign) is close to the point of inversion. Since at the focus the beam has the smallest wall thickness, the axicon can get closer to the point of inversion while avoiding the axicon's tip.

When choosing which axicons to use as the axicon pair there is a variety of different combinations of angles θ and orientations, which will be discussed next.

Axicon pairs with different θ and orientations

Figure 2.14 shows how 4 axicon pairs, that differ only by the orientation of the axicons compared to each other. All four orientation combinations can produce similar magnifications (Fig. 2.14a), which linearly depends on the axicon pair separation. Figure 2.14b shows how the distance between I_1 and I_2 changes with axicon pair separation. Since I_2 is imaged by the projecting components (ML, AC, obj) a shift in its position corresponds to an unwanted defocusing, so for each change of ring size the alignment of the system has to be adjusted. This makes axicon pair combinations with less shift in the position of I_2 (like \gg and $\langle\rangle$ in figure 2.14b) more desirable, since less refocusing is necessary. This refocusing is achieved by adjusting either the position of the projecting optics or the focusing lens.

Figures 2.15 and 2.16 show the situation of axicon pairs with different axicon base angles θ . Here larger θ leads to larger ray angle β (larger $|\rho|$) between the axicons, which means the beam needs less distance to achieve inversion. Also less distance is needed to produce the same range of magnification. This is beneficial when trying to conserve space. Larger $|\rho|$ also means the *control sensitivity* on magnification is greater. Control sensitivity here is defined as how much the diameter of the final ring-shaped potential R is changed by changing the axicon pair separation d by 1 mm:

$$\text{control sensitivity} = \frac{\Delta R}{\Delta d} \quad (2.34)$$

Combining axicons with different θ

The advantage of using 2 axicons with same axicon angle θ is, that axicon 2 decreases ρ by β_0 while axicon 3 increases it again by the same amount, which results in the beam having the same ring divergence ρ before and after the axicon

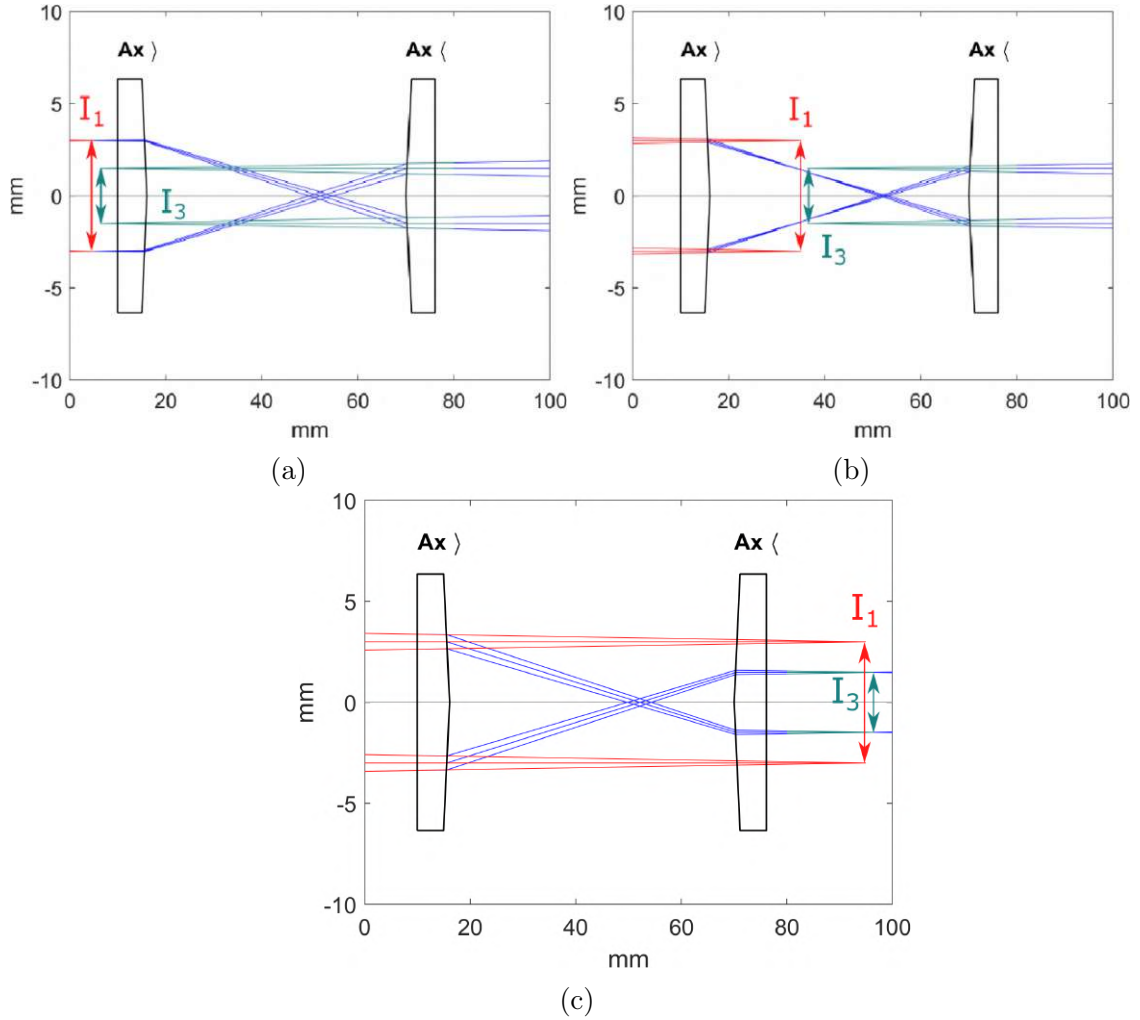


Figure 2.13.: Axicon pair with the tips toward each other: The rays enter from the left side. Depending on the position of the second axicon both the first and second (I_2) intermediate image can be either a real or virtual image. Red rays form I_1 , green rays form I_2 . In (a) I_1 lies before the axicon pair and is a real image, I_2 is virtual. In (b) I_1 lies between the axicons, both images are virtual. In (c) I_1 lies after the axicon pair and is a virtual image, I_2 is real.

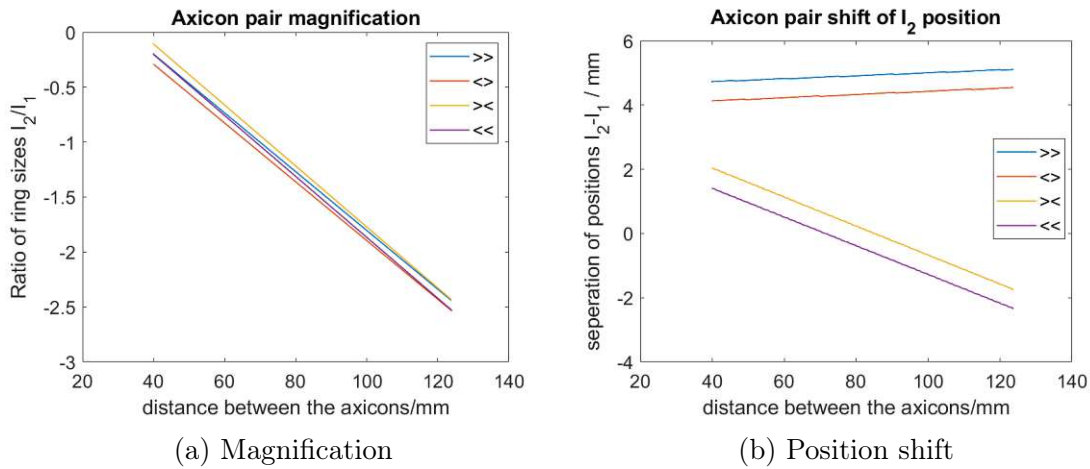


Figure 2.14.: Comparison of the effect of different axicon orientations on magnification (a) and position (b) of the intermediate image created by the axicon pair. The arrows in the legend depict how the axicons are oriented. While all orientation combinations produce similar magnifications, combinations with the last axicon pointing to the right show less shift of the position of I_2 .

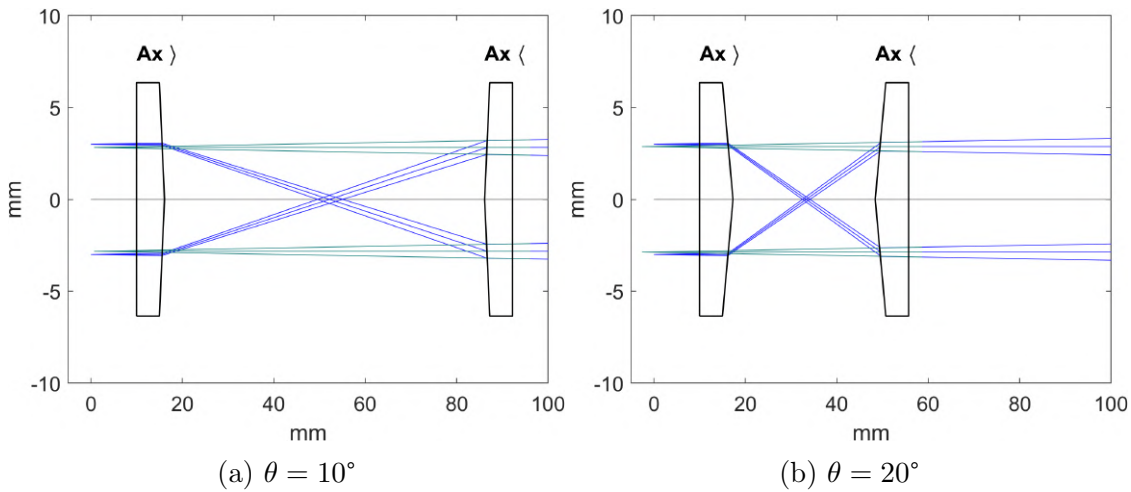


Figure 2.15.: Axicon pairs with different base angle θ : Larger angle θ lets the axicon pair achieve the same magnification in shorter distance, but because the light rays have a larger angle between the axicons 1mm of change in axicon position amounts to a larger change in magnification, increasing the control sensitivity on magnification.

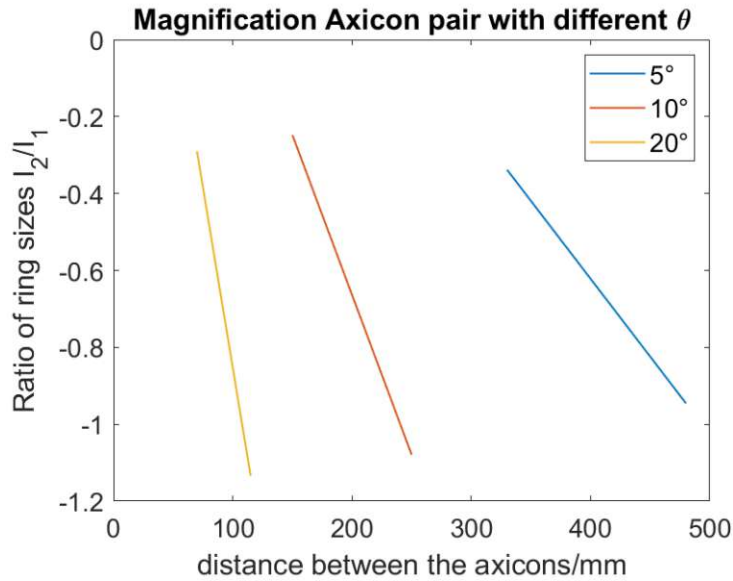


Figure 2.16.: Comparison of axicon pairs with different angles θ : All axicon pairs can roughly cover the same magnification range, but pairs with smaller θ need more distance to do so. The steeper slopes for larger θ indicates smaller control sensitivity.

pair, keeping the beam ‘collimated’. It is possible to design a bit more complicated system that utilizes axicons with different θ . For example, if the focusing lens is positioned, such that ρ is positive after the focusing lens, 2 different axicons could be used to build an axicon pair that results in a beam with $\rho \approx 0$.

The use of the axicon pair enables the key features of the axicon setup. It creates the intermediate image I_2 with sharp inner walls and allows for easily changing the ring size of this image. Finally I_2 needs to be projected onto the atoms.

2.2.3. Pattern projection

To create a sharp ring image at the plane of the atoms the second intermediate image needs to be projected onto the atoms.

In the case of the Lithium experiment the high-NA objective (Special Optics 57-28.1-28), which is used for high resolution imaging, is also used to project the ring image to the atoms. The projection of I_2 should be infinity corrected, because of the design of the objective. To achieve this an achromat can be placed exactly one focal length away from I_2 . In the process I_2 is demagnified by the ratio of focal lengths f_{AC}/f_{Obj} . Because of the limited space available for the system, the choice of achromat is limited, and the combination of AC and Obj can not provide the

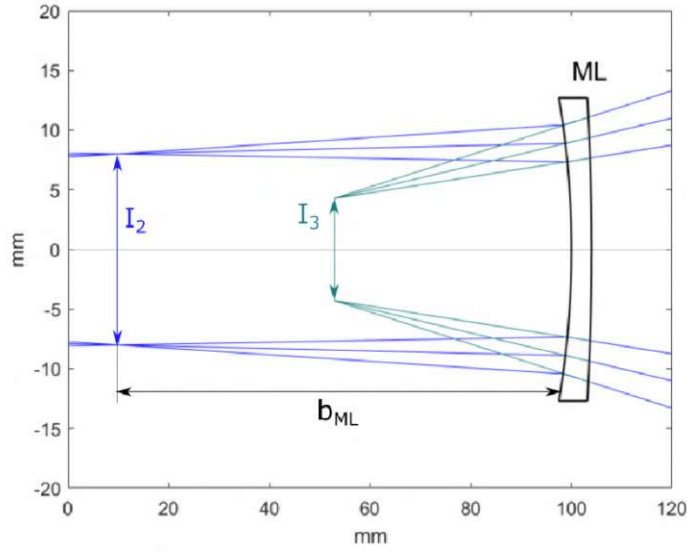


Figure 2.17.: Working principle of the magnifying lens: The second intermediate image I_2 is demagnified and the virtual intermediate image I_3 (green rays) is formed. The magnification depends on the ratio of the distances between the images and the lens d_{I_3}/d_{I_2}

necessary demagnification to achieve small enough ring diameters. To circumvent this limitation a diverging magnifying lens (ML) is introduced, which produces an additional smaller virtual intermediate image I_3 . The additional demagnification depends on the distance to I_2 and the focal length:

$$M_{ML} = \frac{b_{ML}}{f_{ML}} + 1, \quad (2.35)$$

where b_{ML} denotes the distance between the image I_2 and the lens (see figure 2.17).

To reduce aberrations a negative meniscus lens is used instead of a (plano-)concave lens. Using a magnifying lens makes it possible to create small rings, while still keeping the system relatively short. On the downside it increases the wall divergence ω , which will lead to some rays missing the achromat, decreasing the power efficiency of the system.

Refocusing

As mentioned earlier, changing the ring size slightly shifts the position of I_2 and the alignment of the system has to be adjusted to keep a sharp, focused image on the atoms. There are two ways to do this:

- Readjusting the position of ML and AC to shift the focus of the imaging system to the new position of I_2 .
- Adjusting the the position of FL, which shifts I_1 and I_2 . This can be used to move I_2 back to its original position.

While for the first option 2 components need to be shifted, the second option only requires the shift of one component.

To summarize: Axicon 1 creates an diverging ring shaped beam, the focusing lens focuses it and creates I_1 . Then the axicon pair, consisting of axicon 2 and 3 creates I_2 , changing the size of the image depending on the distance of the axicons. The beam inverts between axicon 2 and axicon 3, creating sharp walls on the inside of the ring. Finally the magnifying lens creates the smaller image I_3 , which then can be imaged by the imaging system.

Design Considerations

Here some of the key design considerations of the 3-axicon setup are summarized:

Part	Property	
Axicon 1	larger θ	ring forms earlier (shorter system length) shorter f_{FL} needed to make $\rho \approx 0$
FL	shorter f_{FL}	bigger ω
Axicon pair	larger θ	inversion reached earlier (shorter system length) greater control sensitivity
Axicon 3	Orientation >	less position shift of I_2 , less refocusing needed after ring size change
ML	bigger f_{ML}	less distance needed for same magnification bigger ω
	bigger ω	possible clipping problems, lower power efficiency

2.3. Experimental Setup

The following components were chosen for our 3-axicon setup:

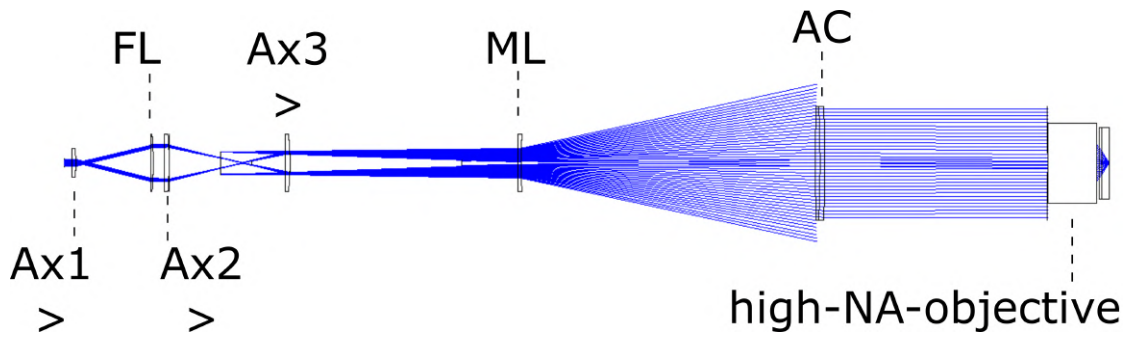


Figure 2.18.: Simulation of the setup in the raytracing software Zemax.

Component	Specifications/Characteristics	Position[mm]
Collimator	Beam waist 1.14 mm Thorlabs F110APC-532	0
Axicon 1	1/2" 10° axicon Thorlabs AX1210-A	10
Focusing lens	1" f = 150 mm plano convex lens Thorlabs LA1433-A	125 - 150
Axicon 2	1" 10° axicon Thorlabs AX2510-A	165
Axicon 3	1" 10° axicon Thorlabs AX2510-A	300-470
Magnifying lens	1" f = -100 mm negative meniscus lens Thorlabs FL1822-A	1065
Achromat	2" f = 300 mm achromat Thorlabs ACT508-300-A-ML	1250

Table 2.1.: Optical components used to build the axicon system

The choice of 10° axicons was made, compromising the requirement of a compact system and good control sensitivity. To achieve $\rho \approx 0$ after the FL f_{FL} has to be smaller than ~ 150 mm or the diverging beam will be bigger than the diameter of the lens before it reaches it. $f_{FL} = 150$ mm was chosen as a compromise, providing a manageably system length, good enough control sensitivity, manageable small ω and resulted in good positioning of the other components, that allowed for efficient use of the space on the breadboard. For the magnifying lens a negative meniscus lens with $f_{ML} = -50$ mm was chosen, because it reduced aberrations and allowed the inner wall to so steep that it is only limited by diffraction.

The high-NA objective together with the 300 mm achromat produce a magnification of 10.8. Together with the magnifying lens the whole imaging system

demagnifies I_2 with a magnification of 90. To avoid vignetting Special optics recommends the distance between AC and the objective to be shorter than 10", so the AC was placed as close to the objective as possible.

2.3.1. Cage system and Layout

The setup is designed in a compact way, while leaving as much space as possible for the DMD-setup. Additionally the vertical space available is limited to < 10 cm. To make alignment as well as moving components (axicon 3 to change ring size and FL to adjust focus) easy, the system was built in a cage. The used components are listed in table 2.2.

Part	Details	
Breadboard	Thorlabs MB3060/M	600 × 300 mm, optical axis 45.3 mm above breadboard
Collimator Mount	Thorlabs KC1L/M	not connected to cage
30 mm cage system	Thorlabs	holds 3 axicons, FL and ML
2 × 1" cage 45° mirror mounts	Thorlabs KCB1C/M KCB1/M	1 mirror back polished for power stabilization
1" cage XY Translator mounts	Thorlabs CXY1A	adjustable mount for all 1" optics (figure 2.19), components mounted in lense tubes and screwed into mount.
2" mirror		glued onto 0.5" mirror mount
60 mm cage system	Thorlabs	holds AC

Table 2.2.: Mechanical components used to build the axicon system

All the components except the achromat are mounted in translation mounts that allow adjusting the position of the component within the mount in 2 directions (figure 2.19). This is crucial for obtaining symmetric rings and a clean image by allowing precise alignment of the optical components relative to each other.

2.3.2. Setting the ring size

To create a ring of a certain size, the position of axicon 3 has to be changed. Then the position of the focusing lens has to be adjusted to keep the image in focus. Additionally the alignment of the focusing lens and axicon 3 can be fine tuned with their respective translation mounts to get the best quality for each ring size.



Figure 2.19.: XY Translation mount CXY1A from Thorlabs used to mount all 1" optics

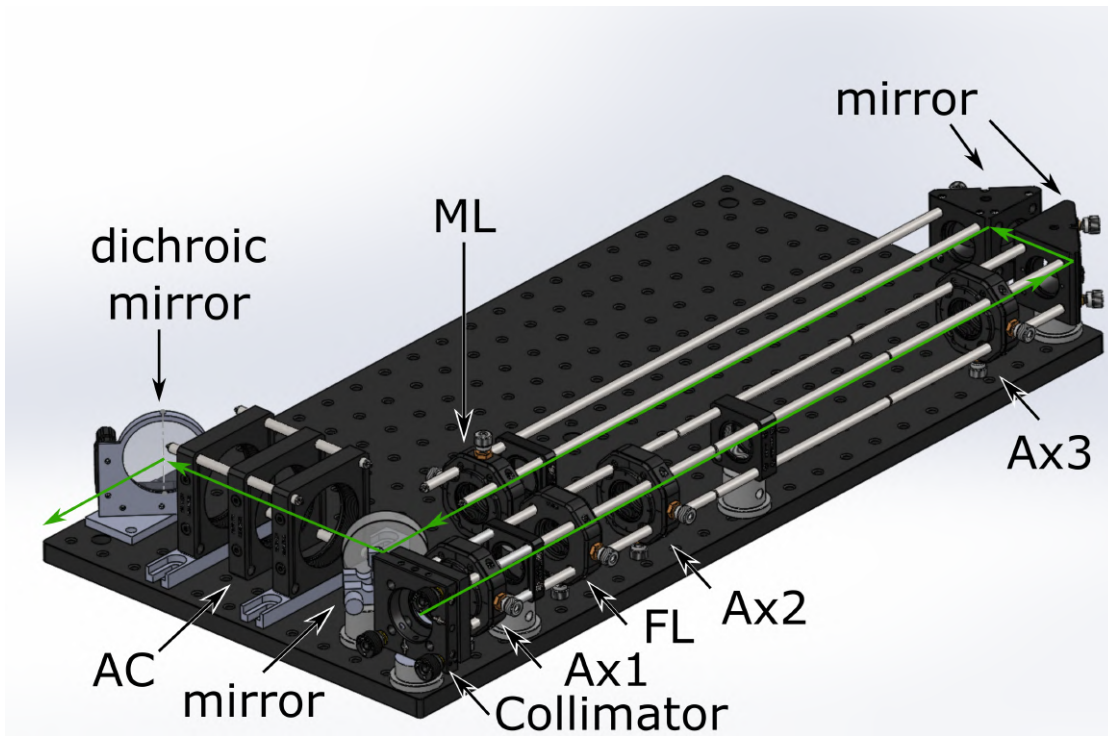


Figure 2.20.: Solidworks-drawing of the axicon setup. The setup is mounted on a 300×600 mm breadboard, which is shared with the DMD setup (chapter 3). The green arrows indicate the path the light takes through the system.

2.3.3. Light sources

The axicon setup uses green 520 nm light. A laser diode (Lasertack LDM-520-140) light source is being tested as this thesis is written. The wavelength is chosen to enable combining the axicon light with the light of the DMD setup (641 nm, see chapter 3) with a dichroic mirror (Thorlabs DMLP567L).

2.3.4. Test setup and Results

In order to test how the system performs, a 200 mm achromat was used as the objective and the rings were imaged onto a camera (ZWO ASI178). As the light source a 641 nm laser (Toptica iBeam smart) was used. All the measured quantities presented in this section are scaled down to give a sense of how big the features of the ring will be in the final setup in the experiment, by scaling them with $\frac{f_{testobj}}{f_{high-NA-obj}}$.

Ring image characterization

After taking an image in the test setup the following analysis procedure is performed: The background noise is subtracted and the position of the ring is detected by cutting the image in the x- and y- directions and detecting the wall peaks and calculating the center. This is then used to inscribe a circle and to extract the minimal wall height H_{min} along the circumference. The image is then binarized with a threshold of $H_{min}/2$ and an ellipse is fitted to the inner wall. From this some characteristics are calculated that are given in table 2.3. The minimal wall height of $1\mu\text{K}\cdot k_B$ is a conservative estimate of the required potential height. In the experimental setup a more realistic requirement would be a minimal wall height of $100\text{nK}\cdot k_B$. The power efficiency relates the optical power outcoupled by the collimator to the optical power that hits the camera.

Having defined how to characterize a ring image, next the results of the test measurements are presented.

System capabilities

Figure 2.21 shows a typical image of a ring, that the system can create. In the crosssection the sharp inner walls can be seen. A collection of ring images with different diameters is given in appendix A. The characteristics of the rings that the system is able to create are given in table 2.4 (for 641 nm light in the test setup). Figure 2.22a shows the linear increase of the ring diameter when the position of axicon 3 is changed. The slope of the linear fit shows a control sensitivity of $1.81\ \mu\text{m}/\text{mm}$. The position of focusing lens needs to be shifted over 2 cm to keep the ring in focus, as can be seen in figure 2.22b. The required power changes from

Quantity	Definition	Goal
diameter D	Mean diameter of the ellipse	$\sim 20\mu m - 200\mu m$
interior darkness	mean intensity in an circle with diameter $0.97D$ in % of H_{min}	$< 1\%$
eccentricity	eccentricity $\sqrt{1 - b^2/a^2}$ of fitted ellipse	
mean wall thickness	mean full width of the wall at $H_{min}/2$	
inner flank thickness	distance it takes the inner wall to rise from 10% to 100% H_{min}	diffraction limited
power	input power needed to create a minimal wall height of $1\mu K \cdot k_B$ for the atoms	$< 100mW$
power efficiency	optical power at the camera divided by the optical power before the first axicon	

Table 2.3.: Characteristics for ring analysis

ring diameter D	23.6 - 253 μm
inner wall flank thickness	$< 0.73\mu m$
mean interior intensity	0.003%
power required for $1\mu K \cdot k_B$	10-45 mW
power efficiency	70-80%
control sensitivity	1.8 $\mu m/mm$ axicon position
wall thickness	2.6-1.9 μm

Table 2.4.: Capabilities of the axicon system

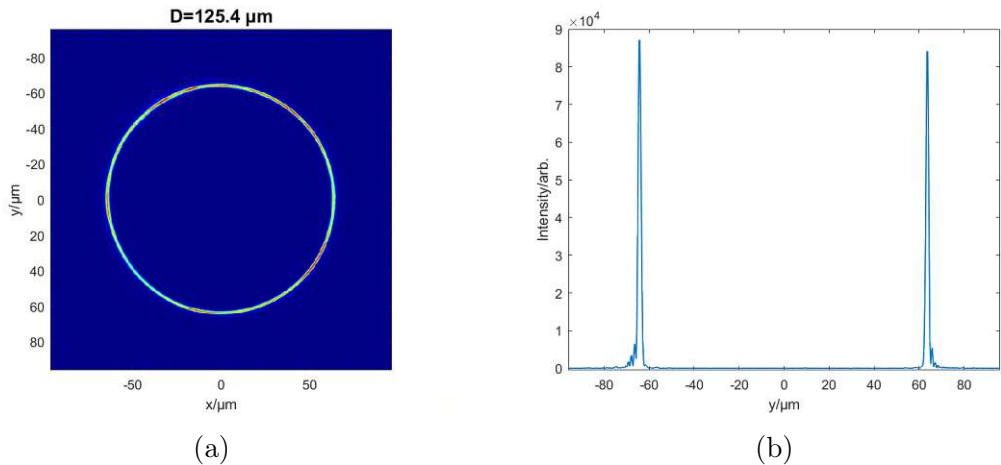


Figure 2.21.: a Ring image with diameter $D = 125.4 \mu\text{m}$. (b) Crosssection through the center of the ring along the y -axis. You can clearly make out the sharp inner walls.

10 to 45 mW for $1 \mu\text{K}$ wall height (figure 2.22c). Figure 2.22d shows the inner wall flank thickness, the diffraction limit is given as a reference. Bigger rings show low eccentricity, but for smaller ring sizes the images get more non-circular (figure 2.22e). The interior of the ring is very dark, the mean intensity is below 0.003% H_{min} for all ring sizes (fig. 2.22f). For smaller diameters the rings become less round and show uneven intensity along the ring (figure 2.23), which is suspected to be caused by imperfections of the axicon's tip.

2.3.5. Technical details

Next I will summarize some details that I encountered while working on the test setup.

Alignment

Having good alignment is crucial for covering a big range of ring sizes and also for creating rings with uniform intensity. Identifying if there are alignment problems in the setup is relatively easy: The beam shape at each point along the beam should be radially symmetric (except for irregularities if axicon 3 is close to the point of inversion) and centered to the cage. It is not so easy though to figure out which component is responsible for the misalignment and which screw needs to be turned to fix it. The following steps describe the alignment scheme used to create rings of good quality:

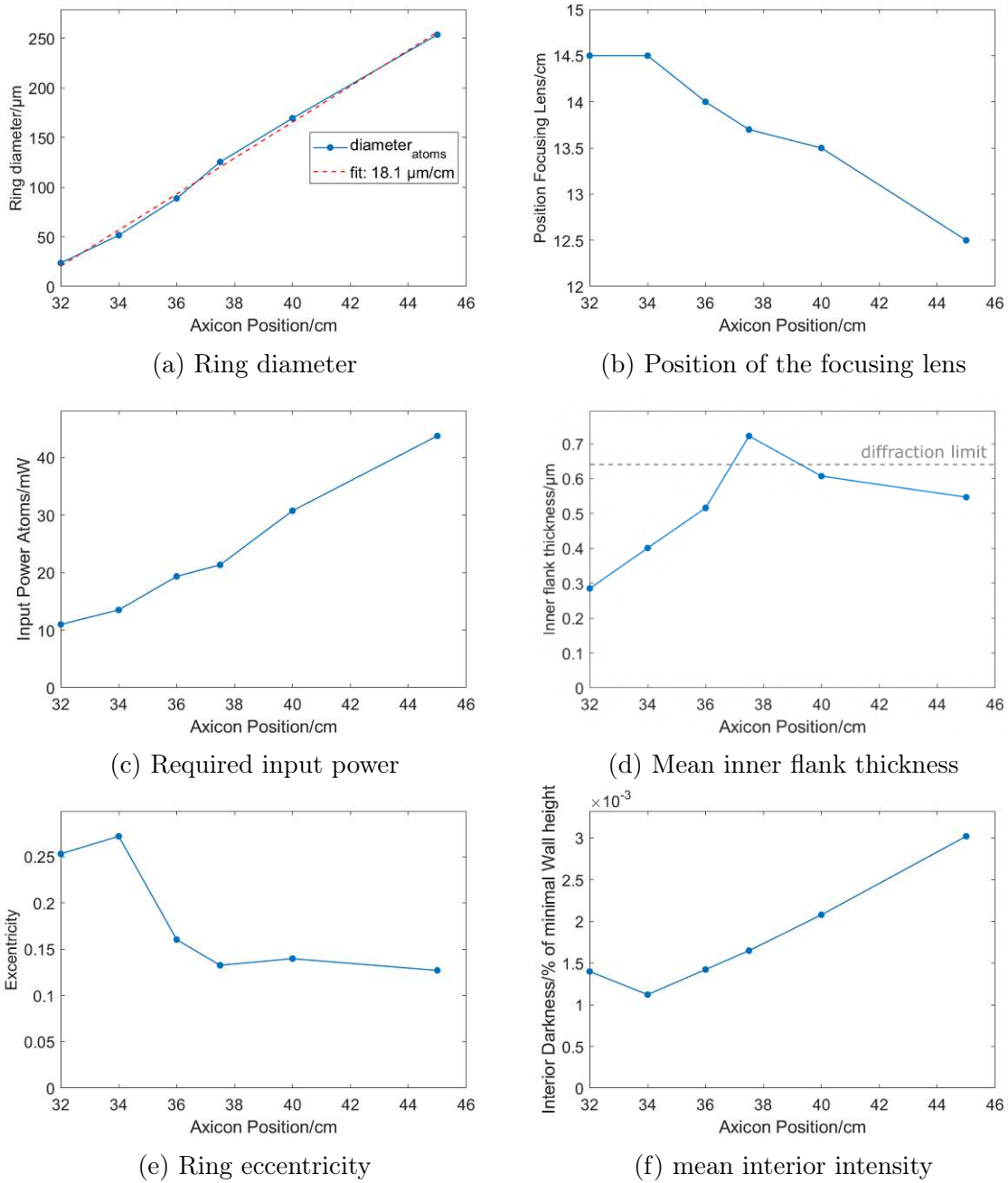


Figure 2.22.: Rings diameter increases linearly with a control sensitivity of $18.1 \mu\text{m}/\text{cm}$. The diffraction limit for the test setup is $0.64 \mu\text{m}$. Required power is given for $1 \mu\text{K} \cdot k_B$ minimal wall height. The images are obtained by subtracting a reference image to eliminate background light. Because of this process the camera noise is not removed and dominates the standard deviation. Therefore the standard deviation of the interior intensity can not be extracted, even though the mean interior intensity can be obtained.

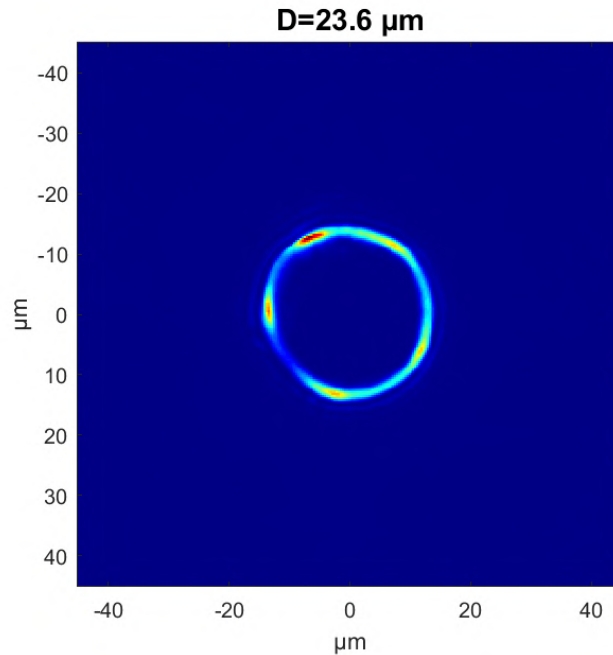


Figure 2.23.: Smallest ring with $D = 23.6 \mu\text{m}$. The ring has become non-circular and shows intensity fluctuations along the wall.

1. The cage is assembled including the translation mounts (CXY1A, figure 2.19), but without the optical components screwed in.
2. The beam is aligned to the center of the cage by using alignment targets (Thorlabs CPA1) and adjusting the kinematic mount of the collimator and the mirrors.
 3. Lenses are added in one by one, starting with the ones farthest away from the collimator (AC \rightarrow CL \rightarrow FL).
 - Each lens is centered with its translation mount before adding the next one.
 4. Axcions are added in one by one, starting with the ones farthest away from the collimator (ax3 \rightarrow ax2 \rightarrow ax1)
 - Each axicon is centered with its translation mount before adding the next one.
 - The axicon can be considered centered when the ring it creates is uniform in intensity. This can be tricky to judge with the naked eye. Shining the beam through a thick piece of paper can make the differences in intensity seem more obvious.
5. After putting in all the components, the positions of the FL and of ax3 can

be further adjusted.

- The shape of the beam at the ML is a good indicator of the quality of the image.
 - Here the beam should look radially symmetric with a bright feature in the center, that is centered to the cage.
6. Additionally the position of ax2 can be further adjusted
 - Here the shape of the beam around the point of inversion is a good indicator for the quality of the image. The beam should look radially symmetric.
 7. If parts of the ring are out of focus on the camera, adjusting the position of the FL can help.
 8. If one side of the ring has drastically less intensity than the other, adjusting ax1 can help.

Bright Spot

During the testing of the setup the occurrence of a bright spot in the center of the ring was encountered (figure 2.24). It turned out it was formed by uncollimated light resulting from an unclean fibre tip. Cleaning the fibre tip got rid of it.

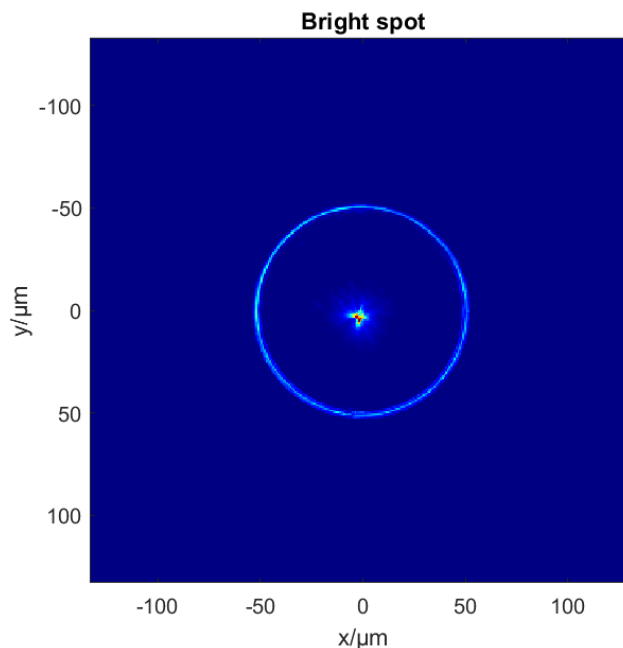


Figure 2.24.: Bright spot in the center of the ring, created by an unclean fiber tip



Die approbierte gedruckte Originalversion dieser Diplomarbeit ist an der TU Wien Bibliothek verfügbar
The approved original version of this thesis is available in print at TU Wien Bibliothek.

3. Creation of tailored and dynamic potentials

In recent years Digital micro mirror devices (DMDs) have been implemented into cold atom experiments to create tailored and dynamic potentials for trapping atoms. There are several different possible approaches [19], in the Lithium experiment the DMD's surface will be directly imaged onto the atoms. The first tests of our DMD, including the choice of the diffraction angles, the characterization of the resolution and defocusing, as well as the design of the laser diode setup for the light source were primarily done by Alexander Braunsberger during a project in our group. Additionally I could heavily rely on the previous work and advice of Mohammadamin Tajik, who during his Master's thesis [20] installed the first DMD to a different experiment in the same research group. Based on this contributions this thesis documents the realization of the DMD setup and the design and implementation of the control software that controls the DMD.

When implementing a DMD into an experiment both the design of the optical setup of the device, as well as the software to control it need to be considered. On the setup side it needs to be factored in, that for some experiments the DMD potential needs to be projected over a large area (up to 1 mm), whereas for others really fine optical resolution is required. The setup needs to provide the flexibility to switch between the two regimes. Because the DMD can only project binary images options for gray-scaling need to be addressed. Furthermore high optical power efficiency is required, since some experiments require high optical power (up to several W). Finally the setup should fit in the available space on the optical breadboard shared with the axicon setup and project the DMD patterns via the existing infinity-corrected high-NA imaging objective (Special Optics, design number 57-28.1-28).

The control software needs to enable projection of both static and dynamic potentials with precise timing and ensure synchronization with the experiment control. Furthermore it should provide additional modes of operation for tasks that do not rely on the experimental cycles, like alignment and projection of patterns for machine learning purposes, like optimal control of the projected pattern.

The following sections will first introduce the DMD and the optical setup that was realized, before detailing how the DMD is controlled and how the DMD control software is structured.

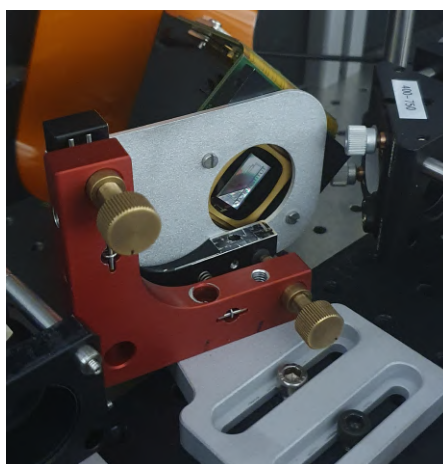


Figure 3.1.: Image of the ViALUX V-9001c mounted in the DMD setup. It is rotated 45° to keep incoming and reflected rays parallel to the optical table. The position of the DMD can be fine-tuned with the red translation mount.

3.1. Digital micro mirror device

A digital micro-mirror device (DMD) consists of an array of micro-mirrors, that can be individually addressed and electro-mechanically controlled [19]. DMDs are commonly used in projectors where they project images onto a screen [19]. A DMD commonly consists of a rectangular array of mirrors. Each mirror is able to flip along its diagonal between two defined positions (On and Off), reflecting incoming light towards these two directions. Additionally the DMD array acts as a 2D blazed diffraction grating, that creates a complex diffraction pattern. There are two different ways of projecting a DMD pattern onto a sample: Fourier and direct imaging. The former projects the Fourier image of the DMD's surface, whereas the later has the DMD array directly imaged onto the atoms. Direct imaging is chosen in the Lithium experiment.

3.1.1. ViALUX V-9001c

The DMD used is the V-9001c from ViALUX that uses a Texas Instruments DLP9000 module. Some important specifications can be seen in table 3.1, for the complete documentation refer to the ViALUX homepage [21] .

Micromirror Array	2560 × 1600 pixels
Micromirror Pitch	7.6 μm
Micromirror Tilt angle	±12°
Active Mirror Array Area	19.4 × 12.1 mm ²
Max Switching rate 1bit	12 987 Hz

Table 3.1.: DMD V-9001c specifications

The DMD has as an IO-Connector to input or output signals. The following pins are used:

Pin	Name	IN/OUT	Description
1	VCC_GPIO	IN/OUT	Sets the I/O Voltage level
7	TRIGGER_IN	IN	Input for external trigger signal
8	SYNCH_OUT	OUT	Synchronization output, one pulse for every frame displayed
10	GND		Power ground

3.2. Optical setup

The DMD pixels rotate around their diagonal. To keep the reflected light parallel to the optical table and thus all optical components in one plane, the DMD is positioned rotated by 45° (see figure 3.1). Since the DMD acts as a diffraction grating, the surface does not merely reflect the input light, but many diffraction orders are formed. Because of this care has to be taken when choosing the angle of incidence of the incoming light. While there is some theoretical description of which angles to use, here we opted for a more experimental approach, where different angle combinations were tried out. In the end the following angles were chosen:

$$\begin{aligned}\alpha &= 35^\circ \\ \beta &= 16^\circ,\end{aligned}$$

where α and β are the incoming and outgoing angle of the light with respect to the normal of the DMD surface. In this configuration $\sim 60\%$ of the power gets reflected into the diffraction order used.

To keep the system flexible for different experimental requirements, a lens setup was designed that enables different system magnifications by changing between different lenses. The system is shown in figure 3.2 and consist of three achromats. L2 and L3 form a $\times 2$ telescope. The DMD is placed in the focal plane of L1 and swapping in lenses with different focal lengths enables different demagnification of

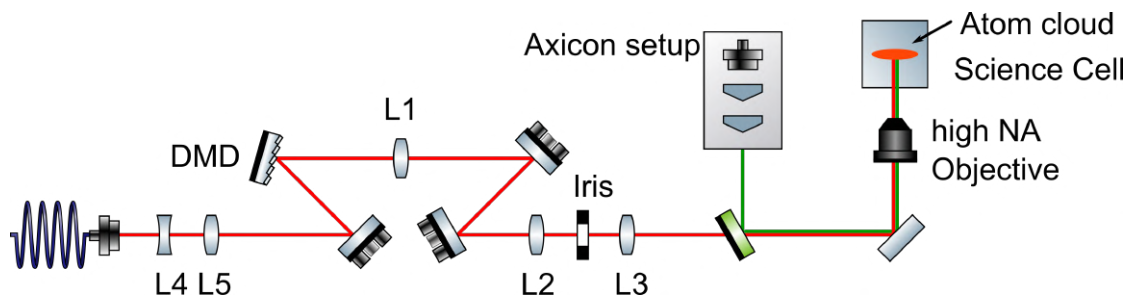


Figure 3.2.: Schematic of DMD setup: L4 and L5 form a telescope that adjusts the beam size to illuminate the whole DMD chip. L1, L2 and L3 image the DMD surface together with the objective. Different focal lengths can be implemented for L1 to achieve different magnifications. $f_{L2} = 75$ mm and $f_{L3} = 150$ mm form a $\times 2$ telescope. The beam gets combined with the green light from the axicon setup via a dichroic mirror. It passes another dichroic mirror before passing through the objective and reaching the atoms in the science cell.

f_{L1}/mm	Demagnification	Projected chip size/ μm^2	pixels per diffraction spot
150	10.8	1796×1120	0.9
250	18	1077×672	1.6
400	28.8	673×420	2.4

Table 3.2.: Demagnification properties of the DMD setup with different lenses L1. The quantities were calculated for the final setup including the high-NA objective (NA = 0.5) and a wavelength of 641 nm.

the DMDs surface. The calculated values for demagnification, projected chip size and the number of pixels per diffraction spot are shown in table 3.2. The lenses L4 ($f_{L4} = -100$ mm) and L5 ($f_{L5} = 125$ mm) form a telescope to match the beam size from the collimator (Thorlabs F810FC-635, beam diameter 6.7 mm) to the size of the DMD chip to illuminate it optimally. After passing through the lenses the light is combined with the light from the axicon setup by a dichroic mirror (Thorlabs DMLP567L).

Gray-scaling

Because of the binary nature of the DMD pixels, where light is either reflected to the atoms or not, it can only produce binary patterns. This limitation can be circumvented by using spatial or time averaging. For **spatial averaging** the DMD array is projected with a setup such that the resolution spot size is larger than the size of a single pixel, hence there are several pixels that contribute to the brightness

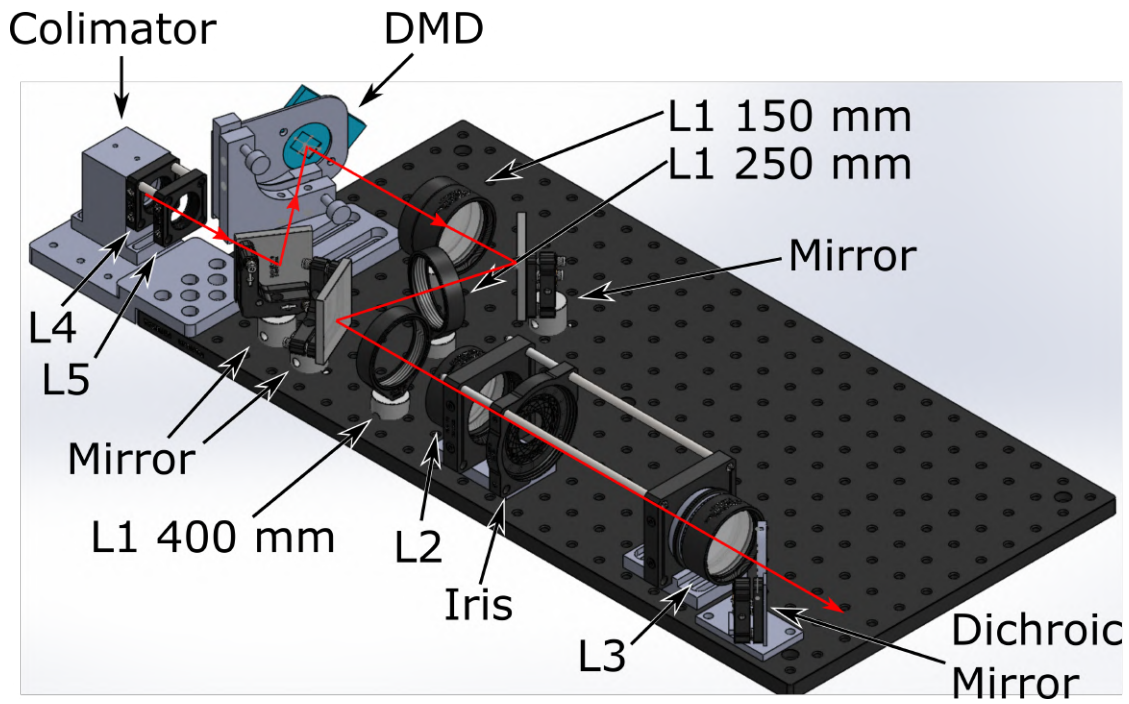


Figure 3.3.: Solidworks-drawing of the DMD setup. The setups is mounted on a 300×600 mm breadboard, which is shared with the axicon setup (chapter 2). The red arrows indicate the path the light takes through the system.

of a diffraction spot. This can be achieved by choosing the demagnification by the choice of lenses, as well as by decreasing the numerical aperture of the system, which can be done by closing the iris that sits inside the telescope L2-L3. For **time averaging** the DMD mirrors can be toggled rapidly to create a time averaged signal. The switching speed here has to be fast compared to the timescale of the atoms. For simplicity only spatial averaging was implemented in our setup. Time averaging might follow in the future after further investigations.

Light source

The DMD setup uses red light which is coupled into an optical fibre. There are currently two different light sources being tested. Toptica iBeam smart ($\lambda = 641$ nm) will be used for low power applications up to 200 mW. For higher power applications a laser diode (Ushio HL63623HD, $\lambda = 638 \pm 6$ nm, 1.5 W) with a cylindrical lens for beam shaping is used. Earlier tests by Alexander Braunsberger showed significant speckle being created by the setup. To remove it the coherence of the incoming light needs to be reduced [22]. To achieve this, methods involving a square-core fibre for mode scrambling and an acousto-optic deflector for shaking of the beam angle are currently being investigated, as this thesis is written.

3.2.1. Test setup

The setup was tested with a 750 mm achromat in place of the high NA-objective. Toptica iBeam smart was used as a light source and the images were taken with a DaHeng Mercury 2 MER2-1220-32U3MC camera. Figure 3.4 shows a 10×10 pixel checkerboard pattern on the DMD, projected with $f_{L1} = 400$ mm. The speckle pattern is clearly visible. Figure 3.5 shows the same projected pattern (400×400 pixels TU Wien logo) with the 3 different lenses L1. To average out the speckle pattern each image is an average over 100 images with different speckle patterns.

3.3. DMD operation and control program

To perform the required task with the DMD, a custom control software was developed. In the next sections the Application Programming Interface (API) that is used to control the DMD is introduced and the design of the DMD control program is presented.

3.3.1. Introduction to the ALP-4.3 API

The DMD is controlled via the API of the ALP-4.3 Controller suite, which handles the communication with the device. To use the API the header file `alp.h` needs to

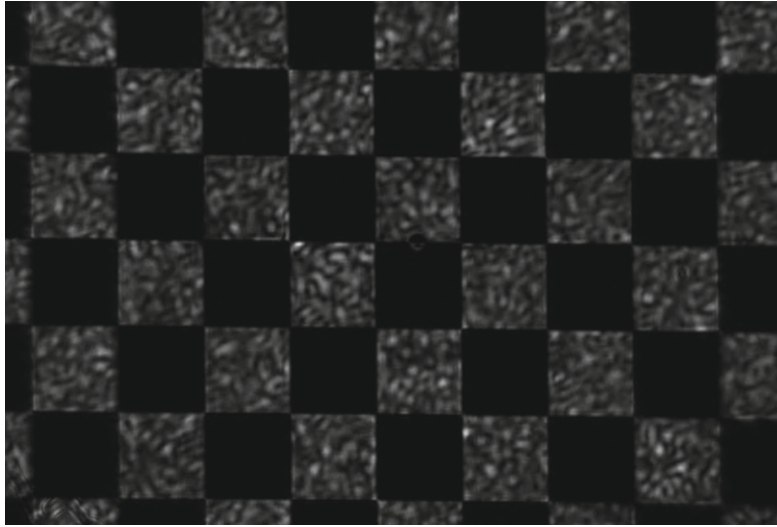


Figure 3.4.: 10×10 pixel checkerboard pattern, $L_1 = 400$ mm. Speckle pattern caused by the interference of coherent light



(a) Projected pattern



(b) $L_1 = 150$ mm



(c) $L_1 = 250$ mm



(d) $L_1 = 400$ mm

Figure 3.5.: 400×400 pixel TU Wien logo projected and imaged with 3 different lenses L_1

<code>AlpDevAlloc</code>	Establishes connection to a ALP device (DMD)
<code>AlpDevControl/AlpDevInquire</code>	Allows for changing / inquiring overall display properties.
<code>AlpDevHalt</code>	Stops current projection and puts DMD into idle state.
<code>AlpDevFree</code>	Frees all DMD resources and disconnects from the device.
<code>AlpSeqAlloc</code>	Allocates memory for a sequence from the DMD RAM.
<code>AlpDevControl/AlpDevInquire</code>	Changes/Inquires the display properties of a sequence.
<code>AlpSeqTiming</code>	Sets the timing properties of a sequence.
<code>AlpProjStart</code>	Starts the projection of a sequence. The sequence is displayed once.
<code>AlpProjStartCont</code>	Starts continuous projection of a sequence. Once all frames have been displayed the sequence starts again from the start.
<code>AlpProjHalt</code>	Puts DMD into idle state after the currently displayed sequence has finished.
<code>AlpProjWait</code>	Waits for the completion of the running sequence display.

Table 3.3.: ALP API functions

be included in the compilation and the library file `alp4395.lib` needs to be linked in the C++ application [23]. In this section all API functions that are used to control the DMD are denoted like this: `AlpSeqStart`. Control parameters that get passed to functions are capitalized (e.g. `ALP_BIN_MODE`). The DMD is controlled by calling the API-functions that are defined in the `alp`-header file. All the available API-functions are listed in the ALP-API description [23], and a short overview with brief descriptions for the most important ones is given in table 3.3.

Terminology

To make it easier to understand the following sections here some terms are introduced:

- `frame`: a 2560×1600 pixel binary (black and white) image
- `sequence`: a collection of one or more frames

- **sequence folder:** system directory in which all the frame files of a sequence are stored
- **cycle:** one experimental cycle
- **request:** a sequence plus timing and other settings. A list of requests is generated at the start of each cycle by the experiment control to be projected during the cycle
- **load:** reading image files from a folder and storing it in the computer system memory
- **put:** transfer of loaded images into the DMD memory using `AlpSeqPut`
- **experiment control:** central control software that manages and coordinates all devices in the experiment
- **DMD control program:** software that manages the DMD operation and controls the DMD. Takes and fulfills requests from the experiment control

The API also allows for gray-scale images which corresponds to time averaging. Since for now only spatial averaging is implemented in the system, only binary frames are used. The API organizes sets of frames projected by the DMD into sequences, each distinguished by a unique sequence ID. When the projection of a sequence is started (by `AlpSeqStart` or `AlpSeqStartCont`) the frames are displayed in the order that they were loaded in. This ordering can be adjusted by the use of a frame look-up table (FLUT). Additionally there are settings available to change on which frame the sequence starts and ends on (`ALP_FIRSTFRAME`, `ALP_LASTFRAME`), as well as to repeat the sequence a certain number of times (`ALP_SEQ_REPEAT`).

3.3.2. Device capabilities and modes of operation

High Speed mode

The 9001c-DMD supports two speed modes:

- standard speed (90 μ s/400 MHz)
- high speed (77 μ s/480 MHz)

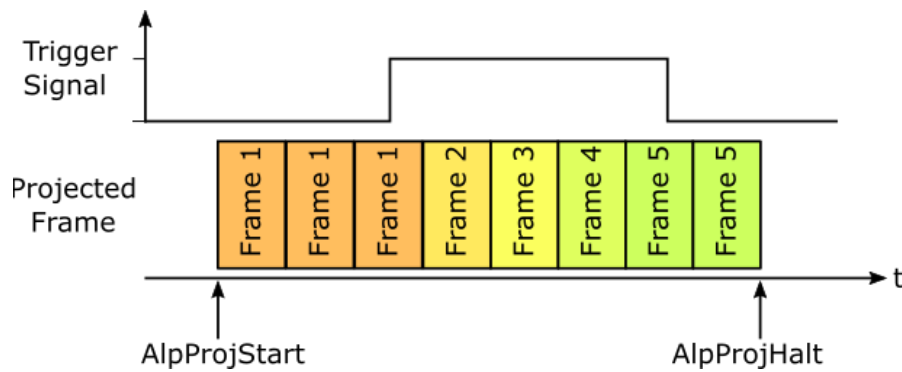


Figure 3.6.: Schematic of frame transition in step mode: Frames are displayed on internal timing. Frame transition to the next frame only when trigger signal is high.

The numbers in the brackets refers to the smallest possible display time of a binary frame, and the maximal switching frequency. The mode is selected by setting `ALP_DEV_DMDTYPE` to either `ALP_DMDTYPE_WQXGA_400MHZ_090A` or `ALP_DMDTYPE_WQXGA_480MHZ_090A`.

Triggers

The projection of frames is controlled by triggers. The DMD offers several different options on how the transition between frames can be triggered:

- internal clock (Master mode)
- external trigger (Slave mode)
- a combination of both (Step mode)

In `ALP_MASTER` mode the DMD relies fully on its internal clock to trigger the frame transition.

In `ALP_SLAVE` mode the transition is triggered by an external trigger signal on the DMDs trigger pin (GPIO Pin 7).

Step mode (`ALP_MASTER + ALP_PROJ_STEP`) allows projection on internal timing with conditional externally triggered frame transition. The DMD will project the frames according to the internal clock, but will only transition to the next frame if a transition condition is met. If this condition is not fulfilled, the current frame will be repeated for the set frame time. The transition condition can be configured to either be a trigger signal (rising or falling flank) or to be a logical signal (high or low). In the DMD program presented in this thesis the transition condition is configured to `ALP_LEVEL_HIGH`, which means the frame transition is triggered if a

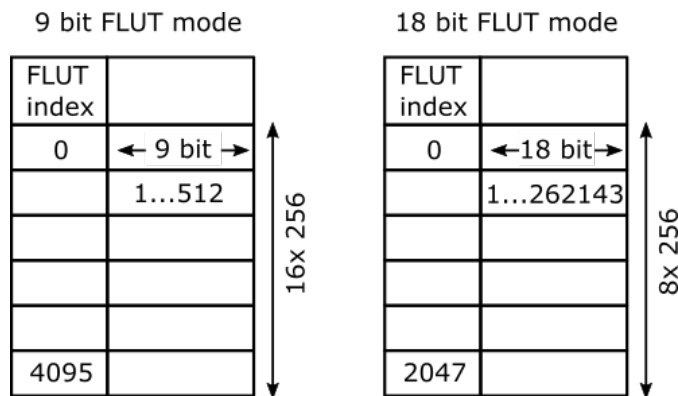


Figure 3.7.: Difference between 9 bit and 18 bit FLUT mode

high TTL-signal is applied on its trigger pin, as is depicted in figure 3.6. From here, whenever external triggering is mentioned in this thesis it is referring to this scenario, where the DMD is configured in step mode and the transition condition is met, by setting the trigger pin signal to high.

Uninterrupted Mode

With standard settings the DMD has a short dark time between two frames. When displaying binary (black and white) images the `ALP_BIN_UNINTERRUPTED` setting can be used to reduce it to zero.

Frame look-up table

The frames of a sequence are put into the DMDs memory sequentially, one after another. This loading order also determines the order in which the frames will be projected when the sequence display is started. Besides this consecutive display the DMD offers ‘random-access’ order via a frame look-up table (FLUT). There is only one FLUT, but different sequences can be configured to access different parts of it by an offset setting. The offset can only be a multiple of 256. The FLUT has a size of 2048 18-bit entries or 4096 9-bit entries depending on the `ALP_FLUT_MODE` setting (see figure 3.7).

Sequence queue

If a sequence is currently being projected another call of `AlpProjStart` allows for putting another sequence into a waiting position. This second sequence is projected once the current one finishes its projection, without any breaks between them (see figure 3.8). With default settings (`ALP_PROJ_LEGACY`) the DMD allows for only one

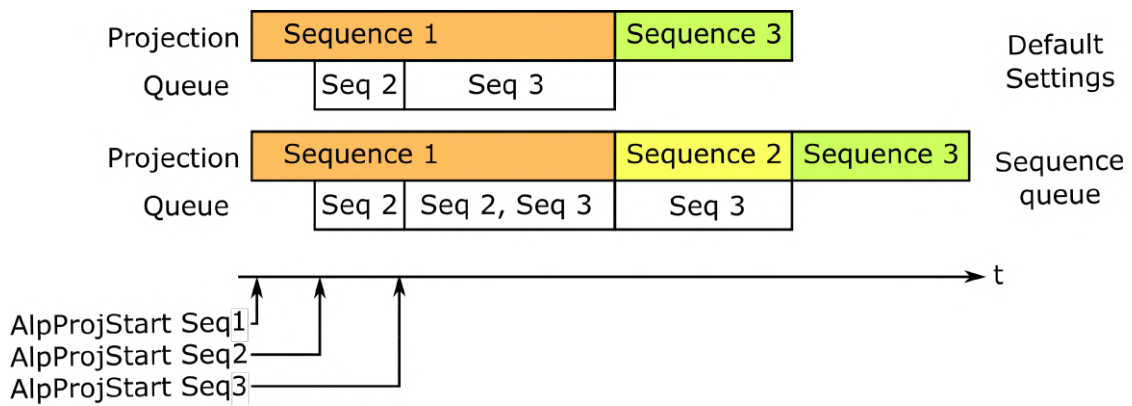


Figure 3.8.: Behavior of waiting sequences with and without the sequence queue. While default settings only allow for one waiting sequence, in sequence queue mode several sequences can be queued up.

waiting position and each subsequent call of `AlpProjStart` overwrites the waiting sequence. `ALP_PROJ_SEQUENCE_QUEUE` mode can be used to put several (more than 1) sequences into a waiting queue. If a sequence is currently projecting, another call of `AlpSeqStart` puts the new sequence at the end of the sequence queue. The queued up sequences start projecting one by one after the current one has finished (figure 3.8). The queue has a finite size. The available queue space can be checked by inquiring `ALP_PROJ_QUEUE_AVAIL`. Settings like `ALP_LASTFRAME` and `ALP_SEQ_REPEAT` still apply.

3.3.3. General Program structure

Since the DMD has the possibility to be used in a huge variety of different experimental procedures within the Lithium experimental setup, a key goal of the design of the DMD control software was to keep and enable this flexibility rather than restrict it. Since the API is written in C++ it was also chosen as the programming language.

The program runs in two threads. One handles the graphical user interface (GUI thread) while the other (worker thread) handles the actual operation, including the communication with the DMD. Both threads communicate via the *qt signals and slots* inter-object communications mechanism of the *qt-library* [24] to e.g. relay user input to the worker.

Worker class

Inside the worker thread an instance of a worker class is created. When user input is detected the GUI thread calls functions of this worker, setting a flag to indicate

that an action was requested by the user. These flags are saved in the workers attributes and the request is fulfilled as soon as possible. To avoid race conditions, where both threads simultaneously try to access the same variables, the specific worker attributes are protected by a mutex¹. The worker manages the different modes of operation. There are currently 3 modes, that will be explained in detail in the next section:

- Continuous: Enables static display of frames for alignment purposes.
- Self-triggered: Displays frames using internal timing without an external trigger.
- Externally-triggered: Used during experimental cycles, where the DMD is triggered via a TTL-signal.

Each mode is implemented as a separate class derived from the *qt QObject* class and is saved in a pair of .h and .cpp files, respectively. This makes it easy to add operation modes in the future by just adding a class. The worker instance runs a loop that checks if any action was requested, by checking its attributes. Whenever the start of a mode is requested it creates an instance of the respective mode class and calls the run()-method. It also relays status updates that the mode emits² to the GUI thread by emitting a *qt-signal*. Each mode establishes connection to the DMD once the run()-method is called and disconnects from the device once the mode operation has finished (by user input or timeout). Additionally the instance of the respective mode class is deleted after the mode has finished.

Sequence class

To reflect the structuring of frames into sequences that the API provides, a sequence class was implemented. This class bundles all the necessary data storage and functionality that handling a sequence needs. All information is stored as class attributes and can be accessed via methods, e.g. all frames in a folder can be loaded by calling the load(folder)-method (see figure 3.9). To make it easier for the reader to distinguish them, different font is used for a sequence (a general collection of frames) and a *sequence* (an instance of the sequence class).

Configuration File

In addition to user input through the GUI, the program also reads information from different files and directories. Both Self-triggered and Externally-triggered

¹mutual exclusion

²emit: is a *qt*-keyword, for creating a *qt*-signal

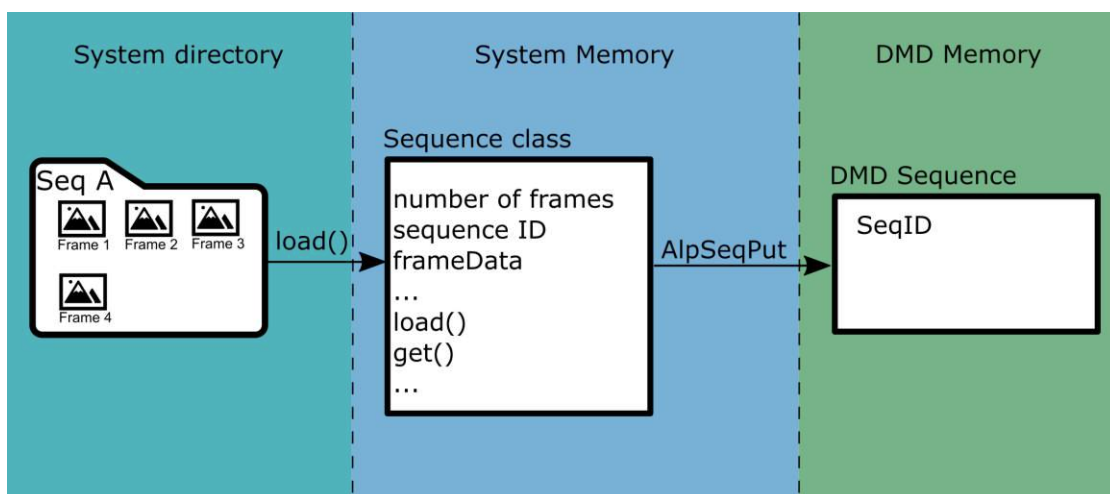


Figure 3.9.: Each frame of a sequence is stored as a .png file in a folder. The sequence is loaded into an instance of a sequence class and stored in the system memory. `AlpSeqPut` is called to transfer the sequence into the DMD's memory.

Setting	ext. trig	self trig
Speed ($77\mu\text{s}/90\mu\text{s}$) =	✓	✓
FLUT (9bit/18bit) =	✓	
Timeout global (s)=	✓	
FrameTime (ms) =		✓
#pix per reload =		✓

Table 3.4.: Config file: Setting requirements for different modes

mode require a configuration file (config file). It initializes general settings for the DMD operations. The different modes require different settings to be defined, as can be seen in table 3.4.

Log File

The program logs status messages, warnings and errors that occur during the operation of a mode in a log file. This file is saved into the log directory that is defined via the GUI. A new log file is created each time a mode starts running.

3.3.4. Modes of operation

The different modes of operation enable the DMD to perform different projection tasks. They require different inputs, like different files and triggers, and are started

via the GUI. Each mode loads frames from directories and expects them to be in the .png format.

3.3.4.1. Continuous display mode

In continuous mode the DMD displays a single image continuously. This is useful to display static images e.g. for alignment purposes.

After establishing connection to the DMD, all .png files in an image folder are loaded into a *sequence* and put onto the DMD. The image folder path is set via the GUI. The program writes a single frame into the FLUT and then uses `AlpProjStartCont` to start continuous projection. The currently projected frame is displayed on the GUI, and the user can change the projected frame by inputting a different index. The program changes the frame by overwriting the FLUT, which can be done without halting projection. The mode ends when a stop is requested by the user.

3.3.4.2. Self-triggered mode

In self-triggered mode the DMD projects all frames from a folder sequentially, without an external trigger. The folder directory is set via the GUI. This mode uses *master mode* and is designed for situations where the DMD projection is separate from the main experiment and a predetermined set of images should be displayed sequentially, e.g. for acquiring a data set for training a machine learning algorithm for pattern optimization. In such a case the sync output of the DMD (GPIO Pin 8) can be used to trigger a camera.

A flowchart of self-triggered mode is shown in figure 3.10. The config file defines a number of N images (#pix per reload, see table 3.4). To display all the .png-images in the image directory the program does not load them all at once, but N images at a time. After initialization and connecting to the DMD, the program prepares 2 *sequences* that are displayed alternately. First N images are loaded into *sequence 1* and projection is started. Then N images are loaded into *sequence 2* and it is added into the queue. The program then waits till *sequence 1* has finished projecting (i.e. the queue being empty), clears it and reloads the next N images while *sequence 2* is being projected. It continues to load N new images into one sequence while the other *sequence* is being projected. The sequences are projected on internal timing, with the frame time being defined in the config file. When less than N images are left, the remaining images are loaded into a third *sequence* that is projected last. Afterwards the memory resources are cleared and the DMD is disconnected.

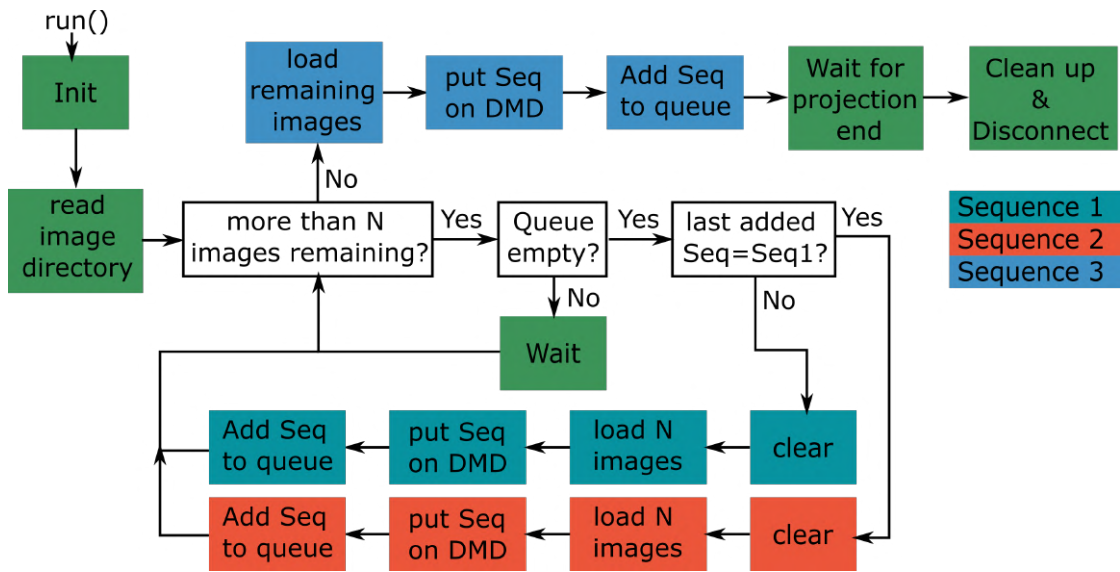


Figure 3.10.: Basic structure of the Self-triggered mode: The turquoise, red and blue boxes refer to *sequences* 1, 2 and 3.

3.3.4.3. Externally-triggered mode

In externally-triggered mode the DMD is configured to load (several) sequences of frames by request of the experiment control, and project them after an external hardware trigger. This will be the regular operation mode of the DMD when used in the experiment. It uses the step mode, uninterrupted mode and sequence queue mode functions of the DMD. The speed, FLUT mode and the global time out parameters can be set in the config file.

Catalog and Request file

In addition to the config file additional files are needed for operation: The **Catalog File** has two functions: Firstly it defines *catalog IDs* that correspond to specific sequence folders. The experiment control uses these ids to request specific sequences to be projected during an experimental cycle. Secondly it sets which sequences should be **preloaded** onto the DMD at the start of operation by the value of the preload flag (0 or 1). The structure of the catalog file is shown in table 3.5 Each line defines a sequence. All .png-frame files within the sequence folder are loaded into a *sequence* in character-by-character lexicographic order of their filenames ($1 < 11 < 2 < A$).

If it is known in advance that certain sequences will be projected during the experiment, or if there are sequences with a high number of frames, preloading can be used to prepare the necessary resources at the start of the DMD operation and

Catalog ID	Path to sequence folder	preload flag
1	C://.../folderSeq1	0
2	C://.../folderSeq2	1
	⋮	

Table 3.5.: Structure of Catalog file

Property	unit/limits	Description
Catalog ID		as defined in the catalog
Time	μs	either duration of 1 frame, or duration of whole sequence depending on Timing Mode
Timing Mode	0/1	0 for frame time, 1 for sequence time
Repetitions	≥ 1	how many times the sequence should be projected
First frame	$1 \dots n_{frames}$	index of the first frame
Last frame	$-1, n_{first} \dots n_{frames}$	index of the last frame, -1 if all frames should be displayed
Reload flag	0/1	1 for reloading the sequence from the sequence folder at cycle start
Frame order	separated by commas	Order in which the frames should be played, 0 for default order

Table 3.6.: Required parameters in a *request* of a sequence by the experiment control

reduce frame loading times between the cycles. If the catalog is modified during the DMD operation, all sequences in both system and DMD memory are discarded and reloaded according to the new catalog. This also happens if the user requests it via the GUI (‘Reload’ button).

At the start of each experimental cycle the experiment control generates a **Request file** that contains a list of *requests*. Each request corresponds to a sequence defined in the catalog file being projected with certain timing and additional parameters. The required parameters are explained in table 3.6. The first and last frame parameters can be used to only project parts of the sequence. The requested frame order is implemented by using the FLUT. If the repetition parameter is greater than 1 the sequence is projected several times back to back. The same sequence can be requested several times per cycle, but for simplicity reasons only one FLUT use (one frame order) is allowed for each sequence per cycle.

Cycle documentation

Additionally to the overall documentation in the log file, a cycle log file is created for each experiment cycle after it has finished. This file documents the projected sequences, including timings, FLUTs and all other relevant settings. In order to have the possibility to reconstruct the exact sequence of frames during an experimental cycle a list of hash values is used to identify the exact frames that were projected.

MD5 hash values To make this frame identification independent of folder and file names each frame gets assigned a MD5 hash value [25] that is generated from its pixel values. Even though the MD5 hashes are not collision free (so 2 different images could produce the same hash, [26]) the probability is low enough for our use-case.

The **library folder** stores a single copy of each unique frame that is ever loaded by the software. The **library file** acts as an index and connects the hashes with the corresponding file path in the library.

Whenever a frame is loaded, its MD5 hash is crosschecked with the library file, and if the frame is not in the library already, it is added as a new entry.

Generating hashes for a large number of images can be computationally expensive and consumes time, which could cause timing problems when executed during the experimental cycles. To generate the hashes in advance, **prehashing** can be requested by the user via the GUI ('Prehashing' Button). Once a hash value has been computed for a frame file is then stored in the filename with naming convention "filename_#md5hash#.png", so the hash calculation does not have to be repeated the next time the file is loaded.

Program operation in externally-triggered mode

A chart of the overall structure of the program is depicted in figure 3.11. Detailed flow charts are given in appendix B.

After starting, the program initializes (connects to the DMD, prepares *sequences* and log files) and then preloads the sequences specified in the catalog file. It then waits and checks in the request directory (defined by GUI) if a new request file is created, which indicates the start of an experimental cycle (blue box). During the waiting preloading or prehashing requests by the user can be fulfilled.

A detailed flowchart of the program operation during an experimental cycle is shown in figure 3.12. At the start of a cycle the software reads the request file and determines if all the necessary sequences to fulfill the request are stored on the DMD already. If not, or if a certain sequence has its reload flag set in the request file, the sequence is (re-)loaded and put onto the DMD. After the FLUT is

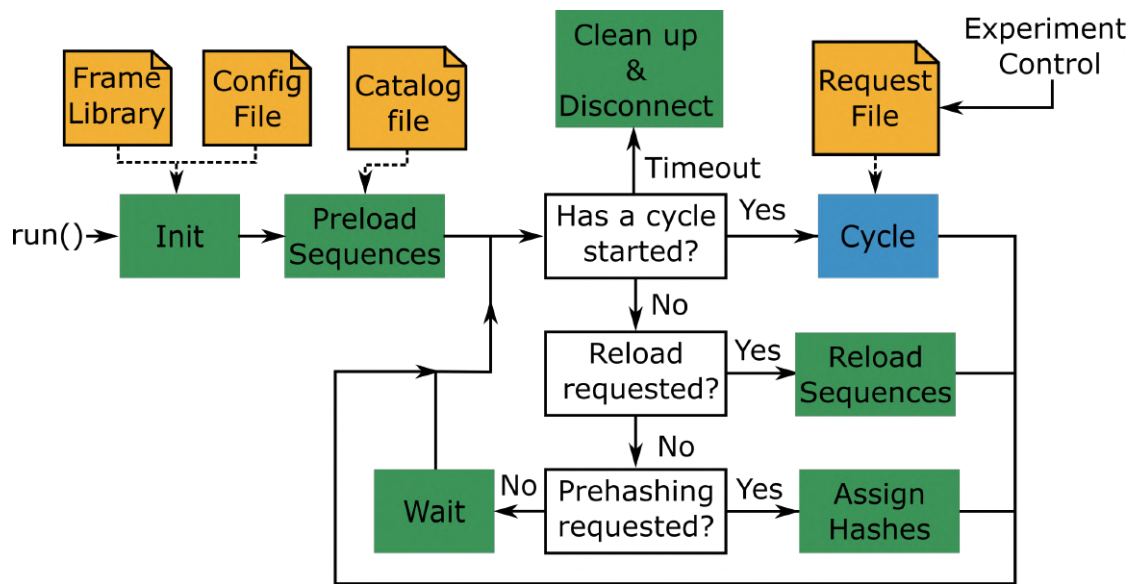


Figure 3.11.: Basic structure of the externally triggered mode

constructed, FLUT-, timing- and other settings are applied and the sequences are put into the queue (sequence queue mode, compare figure 3.8). The DMD then waits for the trigger signal. Once it arrives the queued sequences are projected. The program waits until the queue is empty (the last sequence is being projected) and deploys the projection halt command (`AlpProjHalt`), which puts the DMD into an idle state after the last sequence is done projecting. After this, the cycle is documented, by writing the cycle log file. The program then returns to its waiting state. If the program waits longer than the timeout duration (set in config file), or a stop is requested by user input, the DMD and memory resources are released and the mode terminates.

Important handling notes: It is important to understand that the projection of the first frame of the first sequence starts immediately when `AlpSeqStart` is called. This generally happens before the DMD receives the trigger (see figure 3.6). The DMD will continue to project this first frame until the trigger arrives. It is the *responsibility of the user* to make sure that this first frame is all black, so no unwanted light get projected to the atoms.

3.3.5. Graphical User Interface

The DMD control program is accessed via a graphical user interface (GUI). The GUI was designed using the *qt-library*. The GUI window is shown in figure 3.13. The mode can be selected via a drop-down menu. Each mode has a slightly

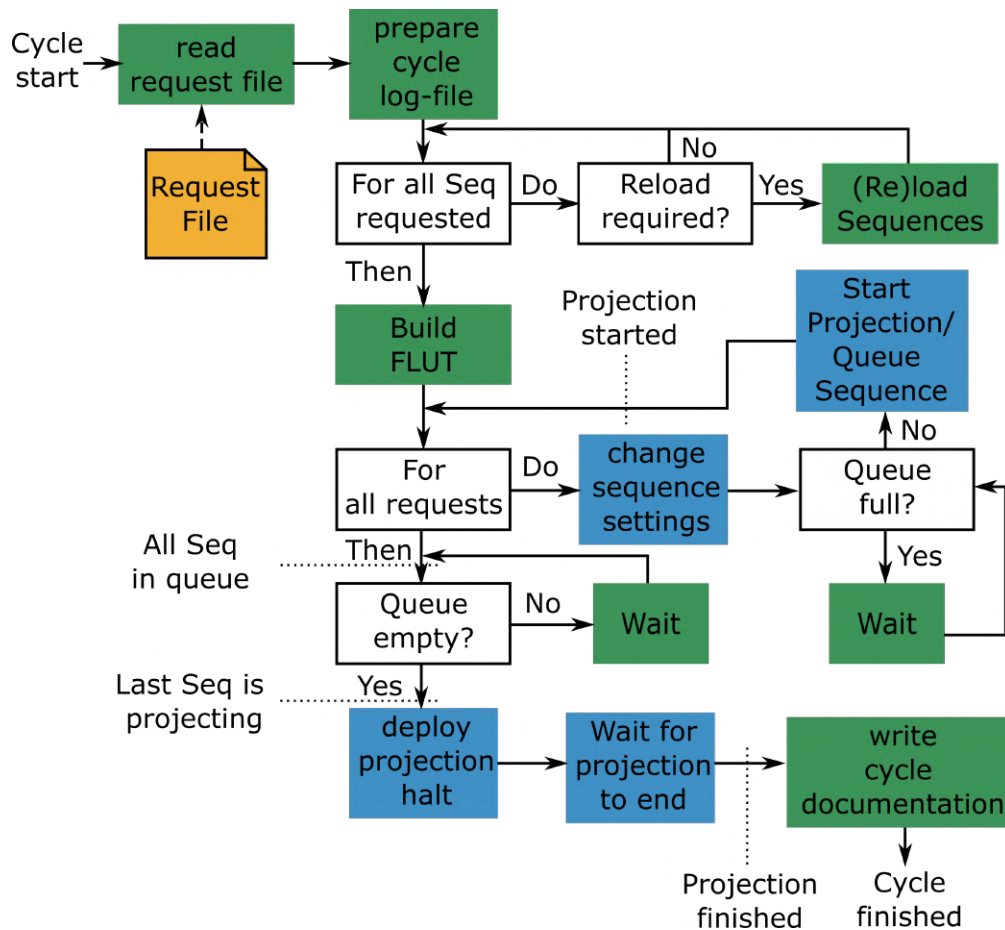


Figure 3.12.: Program structure during an experimental cycle in externally-triggered mode: Blue boxes indicate that API-functions were used in this step to communicate with the DMD.

different appearance, depending on which inputs are needed of its operation.

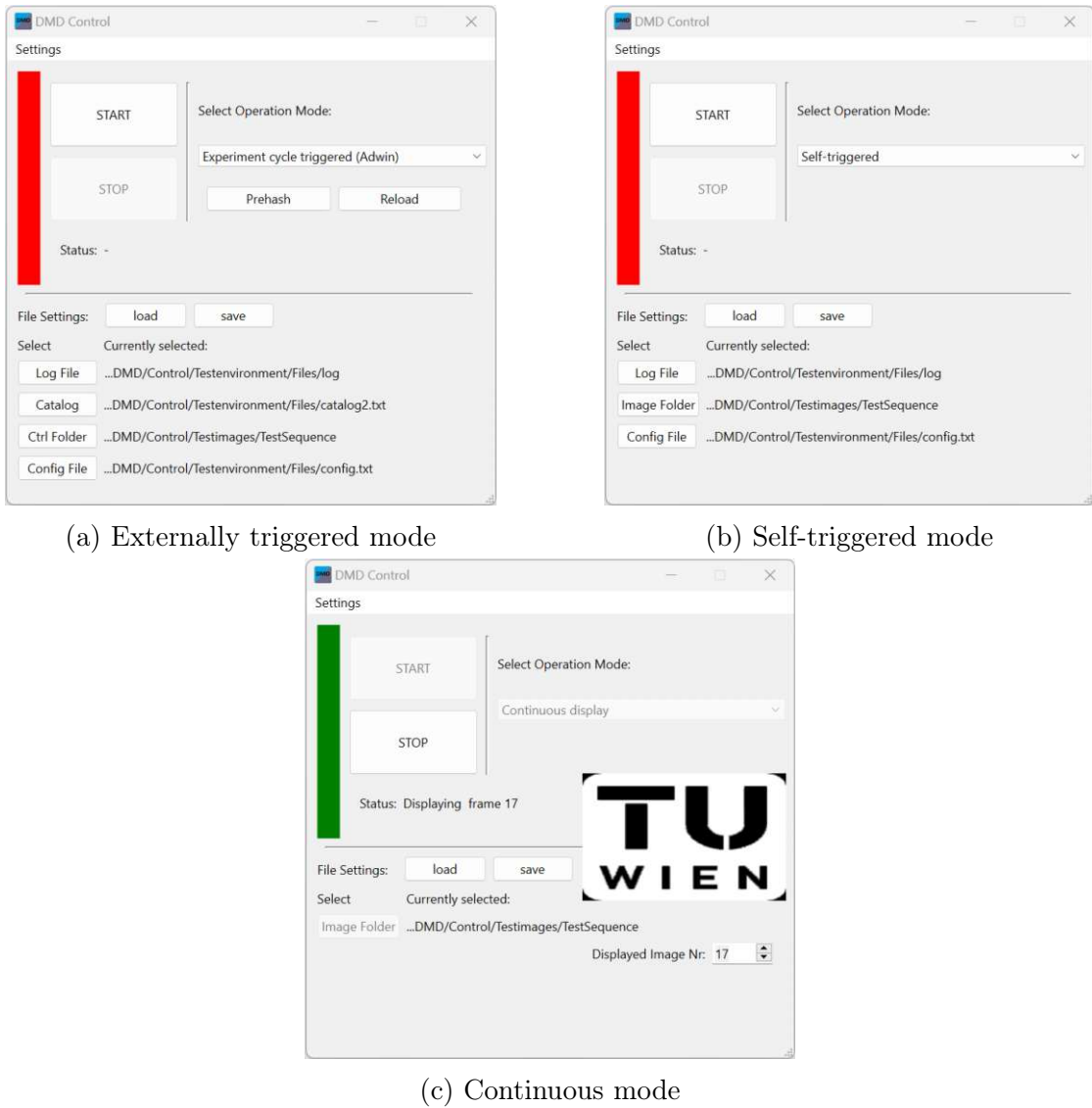
The 'Start' and 'Stop' buttons initiate the starting and stopping of a mode. Below the 'Stop' button the current status of the DMD is displayed. The colored box next to the buttons signals if a mode is currently running or not (red - program idle, green - mode is running). In the lower part of the window necessary files and directories can be selected. The program remembers the last file locations used and loads them on program start. Additionally the current file and directory paths can be saved and loaded again later with the respective buttons. The library directory can be changed by clicking 'Settings' in the menu bar. Buttons and displays are hidden if they are not necessary for a specific mode and are locked during the DMD operation.

In externally-triggered mode a 'Prehash' and a 'Reload' button are displayed to request the respective actions.

In Continuous mode the currently projected frame is displayed, as well as a number box, where the current projected frame can be changed by entering a number, or using the arrow buttons.

3.4. The combined axicon and DMD setup

Both DMD and axicon setup were installed to the same optical breadboard. Figure 3.14 shows the solidworks drawing of the full setup, figure 3.15 shows an image of the system.



(a) Externally triggered mode

(b) Self-triggered mode

(c) Continuous mode

Figure 3.13.: Graphical User Interface: The ‘Start’ button initiates the DMD operation. The color bar to its left indicates if the DMD is currently in use. The ‘Stop’ button ends the current running mode at the next opportunity (e.g. after finishing a cycle in externally-triggered mode). The current status of the DMD is displayed below the ‘Stop’ button. The necessary files and directories for each mode can be selected via their respective buttons (e.g. ‘Log File’) in the bottom half of the window. The program always saves the last set of file directories used and loads them at program start. Additionally they can be loaded and saved via the File setting ‘load’ and ‘save’ buttons. The library directory can be changed by clicking on ‘Settings’ in the Menu bar at the top of the window. In continuous mode the currently displayed frame is shown in the window. It is possible to zoom in by using the mouse wheel.

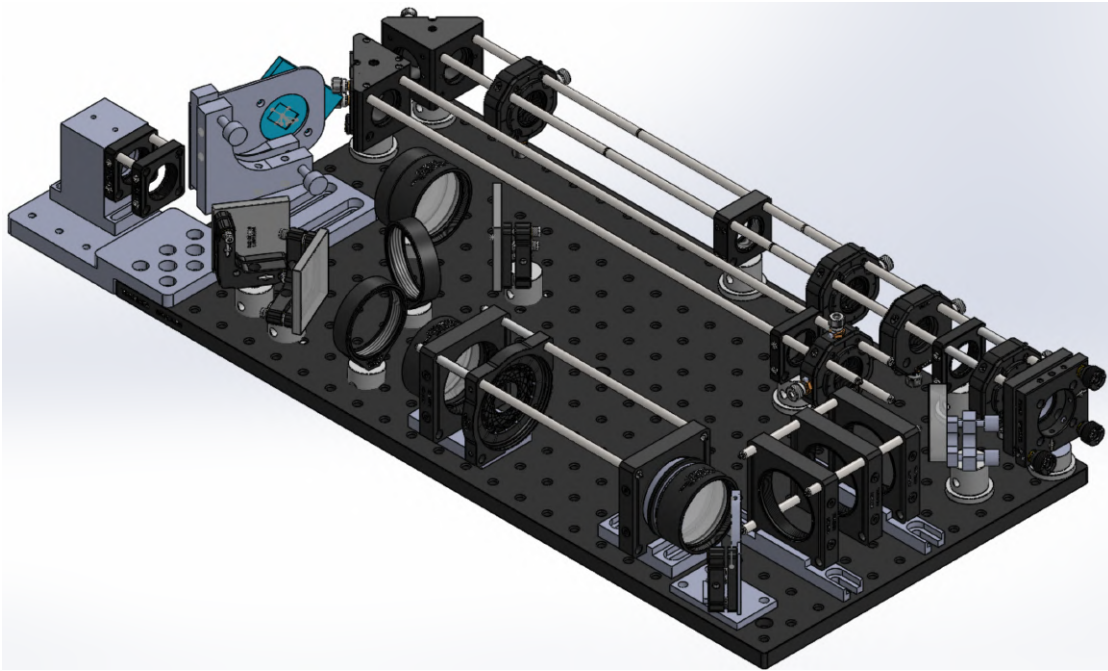


Figure 3.14.: Solidworks drawing of the combined axicon and DMD setup

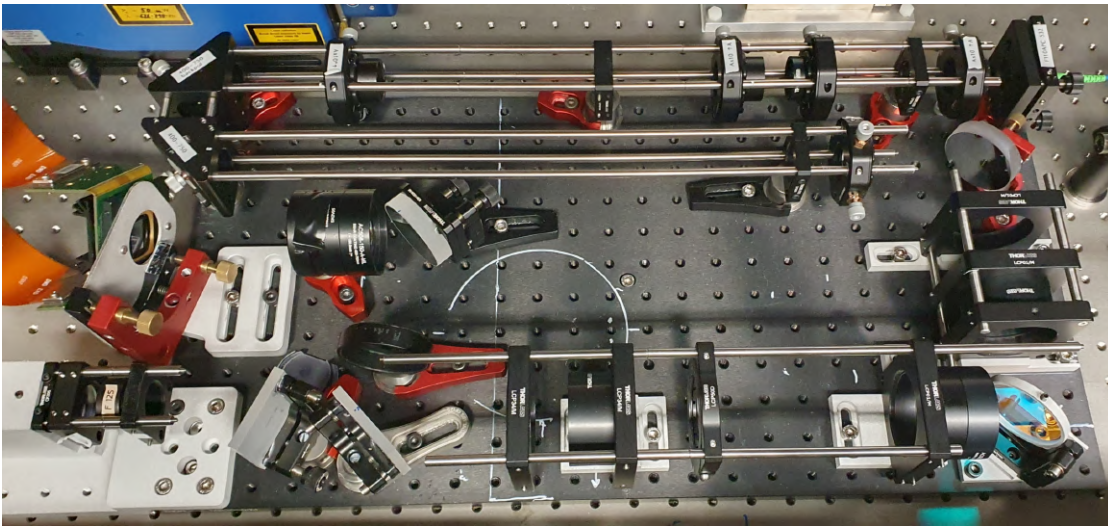


Figure 3.15.: Image of the fully assembled axicon and DMD setup



Die approbierte gedruckte Originalversion dieser Diplomarbeit ist an der TU Wien Bibliothek verfügbar
The approved original version of this thesis is available in print at TU Wien Bibliothek.

4. Conclusion and Outlook

I have established a combined optical system that will be used to realize potentials for upcoming experimental studies in the Lithium system. More accurate ray-tracing matrices for axicon lenses have been introduced and a 3-axicon setup capable of producing variable ring sizes between 23.6 and 253 μm has been constructed, and the patterns characterized. The DMD is also deployed in the combined setup and in particular a versatile control software has been created, which enables operation with experimental cycles or pattern optimization.

Before the system is integrated into the experiment the patterns created by the DMD need to be further examined and characterized. Resolution and gray-scaling need to be quantified. A further possible extension would be the implementation of gray-scaling by time averaging.

Preparation and tests of the light sources of both setups are in progress. The speckle pattern from the DMD need to be addressed. For this beam-shaking by a acousto-optic device is being prepared.

Currently we are working with Martino Calzavara (PGI-8, FZ Jülich) and Andreas Deutschmann-Olek (ACIN, TU Wien) on 2D pattern optimization by machine learning.

Once the system is integrated into the experiment it will be a key ingredient for performing new experiments in 2D and 1D gases for the search of universal dynamics and complex non-equilibrium phenomena.



Die approbierte gedruckte Originalversion dieser Diplomarbeit ist an der TU Wien Bibliothek verfügbar
The approved original version of this thesis is available in print at TU Wien Bibliothek.

Bibliography

- [1] Immanuel Bloch, Jean Dalibard, and Wilhelm Zwerger. Many-body physics with ultracold gases. *Reviews of Modern Physics*, 80(3):885–964, July 2008. ISSN 0034-6861, 1539-0756. doi: 10.1103/RevModPhys.80.885. URL <https://link.aps.org/doi/10.1103/RevModPhys.80.885>.
- [2] Cheng Chin, Rudolf Grimm, Paul Julienne, and Eite Tiesinga. Feshbach resonances in ultracold gases. *Reviews of Modern Physics*, 82(2):1225–1286, April 2010. ISSN 0034-6861, 1539-0756. doi: 10.1103/RevModPhys.82.1225. URL <https://link.aps.org/doi/10.1103/RevModPhys.82.1225>.
- [3] S. Jochim, M. Bartenstein, A. Altmeyer, G. Hendl, S. Riedl, C. Chin, J. Hecker Denschlag, and R. Grimm. Bose-Einstein Condensation of Molecules. *Science*, 302(5653):2101–2103, December 2003. ISSN 0036-8075, 1095-9203. doi: 10.1126/science.1093280. URL <https://www.science.org/doi/10.1126/science.1093280>.
- [4] S. Jochim, M. Bartenstein, A. Altmeyer, G. Hendl, C. Chin, J. Hecker Denschlag, and R. Grimm. Pure Gas of Optically Trapped Molecules Created from Fermionic Atoms. *Physical Review Letters*, 91(24):240402, December 2003. ISSN 0031-9007, 1079-7114. doi: 10.1103/PhysRevLett.91.240402. URL <https://link.aps.org/doi/10.1103/PhysRevLett.91.240402>.
- [5] M. W. Zwierlein, C. A. Stan, C. H. Schunck, S. M. F. Raupach, S. Gupta, Z. Hadzibabic, and W. Ketterle. Observation of Bose-Einstein Condensation of Molecules. *Physical Review Letters*, 91(25):250401, December 2003. ISSN 0031-9007, 1079-7114. doi: 10.1103/PhysRevLett.91.250401. URL <https://link.aps.org/doi/10.1103/PhysRevLett.91.250401>.
- [6] Wolfgang Ketterle and Martin Zwierlein. Making, probing and understanding ultracold Fermi gases. *La Rivista del Nuovo Cimento*, 31(506):247–422, July 2008. ISSN 0393697X, 0393697X. doi: 10.1393/ncr/i2008-10033-1. URL <https://doi.org/10.1393/ncr/i2008-10033-1>.
- [7] Qi Liang. PhD Thesis, TU Wien, 2024. work in progress, private communication.
- [8] Rudolf Grimm, Matthias Weidemüller, and Yurii B. Ovchinnikov. Optical Dipole Traps for Neutral Atoms. In *Advances In Atomic, Molecular, and Optical Physics*, volume 42, pages 95–170. Elsevier, 2000. ISBN

978-0-12-003842-8. doi: 10.1016/S1049-250X(08)60186-X. URL <https://linkinghub.elsevier.com/retrieve/pii/S1049250X0860186X>.

- [9] M. S. Safronova, U. I. Safronova, and Charles W. Clark. Magic wavelengths for optical cooling and trapping of lithium. *Physical Review A*, 86(4):042505, October 2012. ISSN 1050-2947, 1094-1622. doi: 10.1103/PhysRevA.86.042505. URL <https://link.aps.org/doi/10.1103/PhysRevA.86.042505>.
- [10] G. Gauthier, I. Lenton, N. McKay Parry, M. Baker, M. J. Davis, H. Rubinsztein-Dunlop, and T. W. Neely. Direct imaging of a digital-micromirror device for configurable microscopic optical potentials. *Optica*, 3(10):1136, October 2016. ISSN 2334-2536. doi: 10.1364/OPTICA.3.001136. URL <https://opg.optica.org/abstract.cfm?URI=optica-3-10-1136>.
- [11] Klaus M. Hueck. *A homogeneous, tow-dimentional Fermi Gas - Measurements in Position- and Momentum-Space*. PhD thesis, University of Hamburg, 2017.
- [12] John H. McLeod. The Axicon: A New Type of Optical Element. *Journal of the Optical Society of America*, 44(8):592, August 1954. ISSN 0030-3941. doi: 10.1364/JOSA.44.000592. URL <https://opg.optica.org/abstract.cfm?URI=josa-44-8-592>. Number: 8.
- [13] I Manek, Yu.B Ovchinnikov, and R Grimm. Generation of a hollow laser beam for atom trapping using an axicon. *Optics Communications*, 147(1-3):67–70, February 1998. ISSN 00304018. doi: 10.1016/S0030-4018(97)00645-7. URL <https://linkinghub.elsevier.com/retrieve/pii/S0030401897006457>. Number: 1-3.
- [14] Bing Shao, Sadik C. Esener, Jaclyn M. Nascimento, Elliot L. Botvinick, and Michael W. Berns. Dynamically adjustable annular laser trapping based on axicons. *Applied Optics*, 45(25):6421, September 2006. ISSN 0003-6935, 1539-4522. doi: 10.1364/AO.45.006421. URL <https://opg.optica.org/abstract.cfm?URI=ao-45-25-6421>. Number: 25.
- [15] W. P. Latham. Characteristic analysis of a refractive axicon system for optical trepanning. *Optical Engineering*, 45(9):094302, September 2006. ISSN 0091-3286. doi: 10.1117/1.2353119. URL <http://opticalengineering.spiedigitallibrary.org/article.aspx?doi=10.1117/1.2353119>. Number: 9.
- [16] Zbigniew Jaroszewicz, Anna Burvall, and Ari T. Friberg. Axicon - the Most Important Optical Element. *Optics and Photonics News*, 16(4):34, April 2005. ISSN 1047-6938, 1541-3721. doi: 10.1364/OPN.16.4.000034. URL <https://opg.optica.org/abstract.cfm?URI=opn-16-4-34>. Number: 4.

- [17] Herbert Gross, editor. *Handbook of Optical Systems: Volume 1: Fundamentals of Technical Optics*. Wiley, 1 edition, January 2005. ISBN 978-3-527-40377-6 978-3-527-69922-3. doi: 10.1002/9783527699223. URL <https://onlinelibrary.wiley.com/doi/book/10.1002/9783527699223>.
- [18] Daomu Zhao. The ray transfer matrices for axicons. *Optik*, 110(10):493–494, 1999. Number: 10.
- [19] Guillaume Gauthier, Thomas A. Bell, Alexander B. Stilgoe, Mark Baker, Halina Rubinsztein-Dunlop, and Tyler W. Neely. Dynamic high-resolution optical trapping of ultracold atoms. In *Advances In Atomic, Molecular, and Optical Physics*, volume 70, pages 1–101. Elsevier, 2021. ISBN 978-0-12-824610-8. doi: 10.1016/bs.aamop.2021.04.001. URL <https://linkinghub.elsevier.com/retrieve/pii/S1049250X2100001X>.
- [20] Mohammadamin Tajik. Arbitrary one-dimensional optical dipole potentials on an atom chip. page 58 pages, 2017. doi: 10.34726/HSS.2017.43483. URL <https://repositum.tuwien.at/handle/20.500.12708/3796>. Artwork Size: 58 pages Medium: application/pdf Publisher: TU Wien.
- [21] ViALUX Messtechnik Bildverarbeitung GmbH. SuperSpeed V-Module. Technical report. URL <https://www.vialux.de/de/superspeed-download.html>.
- [22] Scott Patrick Hubele. Potential Shaping Using a DMD and High-Resolution Imaging of Cesium Atoms in Optical Lattices. *Master thesis*, 2022.
- [23] ViALUX Messtechnik+Bildverarbeitung GmbH. ALP-4.3 Controller Suite Application Programming Interface, 2022.
- [24] Qt Documentation. Qt-Signals & Slots. Technical report. URL <https://doc.qt.io/qt-6/signalsandslots.html>.
- [25] R. Rivest. The MD5 Message-Digest Algorithm. Technical Report RFC1321, RFC Editor, April 1992. URL <https://www.rfc-editor.org/info/rfc1321>.
- [26] Philip Hawkes, Michael Paddon, and Gregory G. Rose. Musings on the wang et al. MD5 Collision. In *IACR Eprint archive*. 2004. URL <http://eprint.iacr.org/2004/264>.



Die approbierte gedruckte Originalversion dieser Diplomarbeit ist an der TU Wien Bibliothek verfügbar
The approved original version of this thesis is available in print at TU Wien Bibliothek.

Acknowledgements

My time at the Atominstitut has been eventful and has shaped me greatly, both on a scientific and a personal level. I have to thank Professor Jörg Schmiedmayer for the opportunity of working in his research group and making it a great place for young people to learn and find their way into science. I want to thank RuGway Wu, whose expertise, patience and encouragement have helped me immensely. His guidance and mentorship have significantly shaped my understanding and approach to the project and to physics in general. Furthermore I want to thank the whole Lithium team, Chen Li, Qi Liang, Pradyumna Paranjape and Sebastian Erne, for working with me and providing their help and knowledge.

Next I want to thank Alexander Braunsberger and Oliver Lueghammer for spending many fruitful hours in the lab with me. For his contributions to the DMD setup I have to again thank Alex as well as Mohammadamin Tajik and Yevhenii Kuriatnikov for sharing their knowledge.

I want to thank all my colleagues in the Atomchip group for the warm welcome, their scientific support and the many fun and enriching discussions in the office and the coffee corner. I want to thank the team of the mechanical workshop for their rapid manufacturing of all the parts needed to build the setup and all the other researchers and staff of the Atominstitut that make it a great place to work at.

I want to acknowledge my friends for their unwavering support, many hours of long talks and for accompanying me on my journey through university and life. I am deeply grateful for having you. Special thanks to Nikolaus Hondl for the countless fun hours we spent together repairing his 3D printer.

Last but not least I want to thank my parents, Rudolf and Christine, and my sister. Their enduring support made my studies possible. Thanks for believing in me.

To all those mentioned above, as well as to the countless others who have contributed to my academic journey in ways big and small, I extend my sincerest gratitude. Your support, encouragement, and belief in me have been invaluable, and I am profoundly grateful for each of you.



Die approbierte gedruckte Originalversion dieser Diplomarbeit ist an der TU Wien Bibliothek verfügbar
The approved original version of this thesis is available in print at TU Wien Bibliothek.

A. Ring patterns produced by the axicon setup

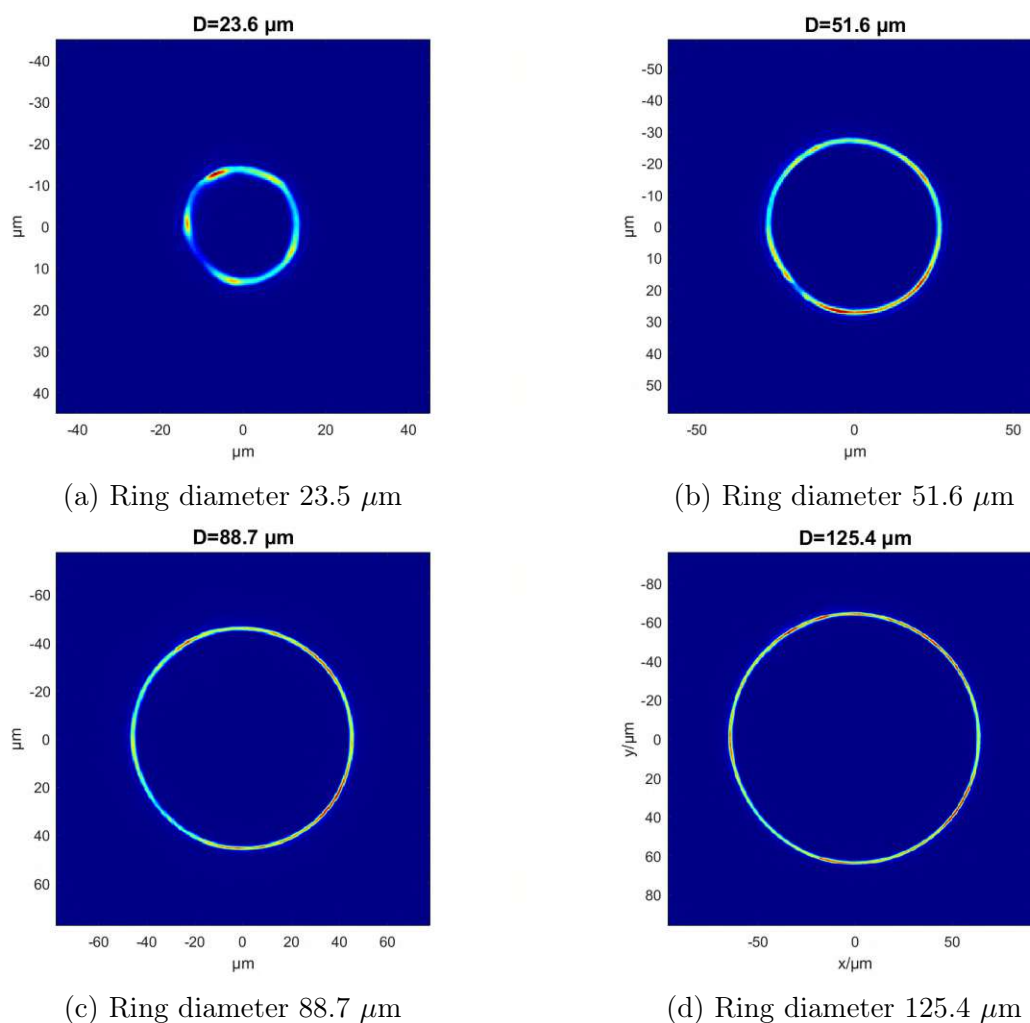
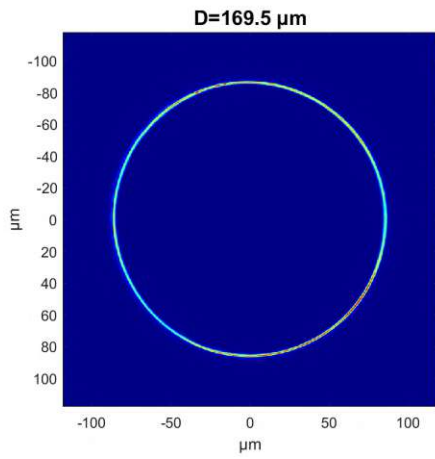
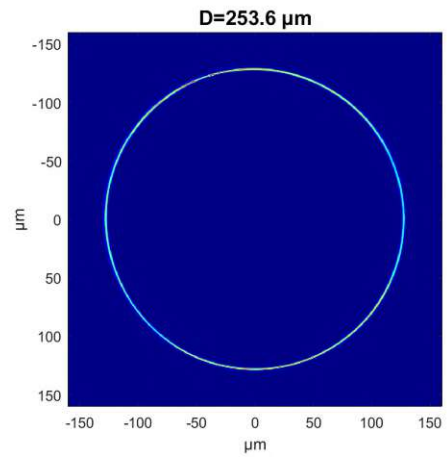


Figure A.1.: Ring images of different size produced by the axicon test setup (see section 2.3.4).



(a) Ring diameter 169.5 μm



(b) Ring diameter 250 μm

Figure A.2.: Ring images of different size produced by the axicon test setup (see section 2.3.4).

B. Flowcharts of externally-triggered mode

